

Particle Re-Acceleration in Colliding Winds Systems? Radio, X-ray, and γ -ray Emission Models of WR 140

J. M. Pittard^{1*} and S. M. Dougherty²

¹*School of Physics and Astronomy, The University of Leeds, Woodhouse Lane, Leeds LS2 9JT, UK*

²*National Research Council of Canada, Herzberg Institute for Astrophysics, Dominion Radio Astrophysical Observatory, P.O. Box 248, Penticton, British Columbia V2A 6J9, Canada*

Accepted ... Received ...; in original form ...

ABSTRACT

We present calculations of the spatial and spectral distribution of the radio, X-ray and γ -ray emission from shock accelerated electrons in the wind-collision region (WCR) of WR140. Our calculations are for orbital phase 0.837 when the observed radio emission is close to maximum. Using the observed thermal X-ray emission at this phase in conjunction with the radio emission to constrain the mass-loss rates, we find that the O-star mass-loss rate is consistent with the reduced estimates for O4–5 supergiants by Fullerton, Massa & Prinja (2005), and the wind momentum ratio, $\eta = 0.02$.

The observed low frequency turnover at ~ 3 GHz in the radio emission is due to free-free absorption, since models based on the Razin effect have an unacceptably large fraction of energy in non-thermal particles. A key result is the index of the non-thermal electron energy distribution is flatter than the canonical value for diffusive shock acceleration (DSA), namely $p < 2$. It is argued that this requires re-acceleration of non-thermal particles in multiple wind-embedded shocks, which are then injected as seed particles for further acceleration at the global shocks bounding the WCR.

There are some tantalizing hints that shock modification occurs in these systems. For example, the estimated amount of energy placed into non-thermal particles is high enough that non-linear effects should be important, and changes in the degree of shock modification with orbital phase may account for the asymmetry of the radio lightcurve and the smaller than expected variation in the X-ray lightcurve. Shock modification also results in softer X-ray emission from the post-shock plasma due to a reduction in the velocity jump across the subshock. While this is also consistent with observations, the long timescale for energy transfer between the post-shock ions and electrons may be the dominant cause.

Tighter constraints on p and the nature of the shocks in WR 140 will be obtained from future observations at MeV and GeV energies, for which we generally predict lower fluxes than previous work. Since the high stellar photon fluxes prevent the acceleration of electrons beyond $\gamma \gtrsim 10^5 - 10^6$, TeV emission from CWB systems will provide unambiguous evidence of pion-decay emission from accelerated ions. We finish by commenting on the emission and physics of the multiple wind collisions in dense stellar clusters, paying particular attention to the Galactic Centre.

Key words: gamma-rays: theory – radio continuum: stars – X-rays: stars – stars: binaries: general – stars: early-type – stars: individual: WR140

1 INTRODUCTION

Massive binary systems containing a Wolf-Rayet (WR) and O-type star often exhibit synchrotron emission arising from relativistic electrons in the presence of a magnetic field (Dougherty & Williams 2000). The non-thermal electrons

are widely thought to be accelerated through diffusive shock acceleration (DSA), though other mechanisms are also possible (e.g., Jokipii 1987; Jardine, Allen & Pollock 1996). High-spatial-resolution observations (e.g., Williams et al. 1997; Dougherty, Williams & Pollacco 2000; Dougherty et al. 2005) have revealed that the acceleration site is the region where the massive stellar winds collide - the wind-collision region (WCR). Thus, colliding-wind binary (CWB) systems

* E-mail: jmp@ast.leeds.ac.uk

present an important laboratory for investigating the underlying physics of particle acceleration since they provide access to higher mass, radiation and magnetic field energy densities than in supernova remnants (SNRs), which have been widely used for such work.

CWB systems are also ideal for understanding related, but more complicated, systems involving colliding winds, such as the cluster of massive stars in the central parsec of the Galaxy (Ghez et al. 2005), and young, dense stellar clusters (super star clusters), such as the Arches (Figer et al. 1999), NGC 3603 (Moffat et al. 2002), and R136 (Figer, McLean & Morris 1999). Non-thermal radio emission has recently been detected from the Arches cluster (Yusef-Zadeh et al. 2003), and the non-thermal radio filaments and “streaks” near the Galactic Centre may have their origin in colliding wind binaries and cluster winds (Yusef-Zadeh 2003).

If the efficiency of particle acceleration at shocks is high, non-linear feedback effects can modify the structure of the shock. The shocks in SNRs are believed to produce the majority of galactic cosmic rays, at least up to the so-called “knee” near 10^{15} eV (e.g., Hillas 2005), and in order to do this they must place ~ 10 per cent of their explosion energy into relativistic ions over their lifetime. The efficiency in young SNRs may be significantly greater than this, and theoretical calculations have shown that the shock structure, the remnant evolution, and its radiative properties may all be modified (e.g., Berezhko, Elshin & Ksenofontov 1996; Decourchelle, Ellison & Ballet 2000). This work is supported by recent analysis of observations of a number of young SNRs, including SN 1006 (Bamba et al. 2003; Berezhko, Ksenofontov & Völk 2003), which provide convincing evidence for the efficient acceleration of non-thermal ions and shock modification. Further observational support that collisionless shocks can accelerate particles with high efficiency comes from direct spacecraft measurements of the Earth’s bowshock and interplanetary shocks (see references in Ellison & Cassam-Chenaï 2005). An unresolved question is whether or not DSA is efficient at the high energy densities which exist in CWB systems.

In this paper we model the thermal and non-thermal radio, X-ray and γ -ray emission from one of the wider CWB systems, WR 140. In Sec. 2 we describe our modelling of the radio emission, including several cooling processes, and various emission and absorption mechanisms. Sec. 3 contains details of our models of the non-thermal X-ray and γ -ray emission. The application of our model to observations of WR 140 is described in Sec. 4, and the implications of our modelling are discussed in Sec. 5. In Sec. 6, we summarize and note future directions.

2 MODELLING THE RADIO EMISSION

Our calculations of the observed radio emission from CWB systems are based on the density and temperature distribution obtained from 2D hydrodynamical simulations of the stellar winds and their collision (see Dougherty et al. 2003; Pittard et al. 2006). In this model, both the stellar winds and the WCR contribute thermal emission and absorption. The free-free emission and absorption coefficients are determined from the local temperature and density values on the

hydrodynamic grid. In order that the non-thermal emission may be modelled, the population and spatial distribution of non-thermal particles must be specified.

It is expected that the second-order Fermi mechanism will be less efficient at accelerating particles than DSA, since in our models the pre-shock Alfvénic Mach number, $M_A = v\sqrt{4\pi\rho}/B \gtrsim 3$ - see Table 1. Particles might also be accelerated at the contact discontinuity between the two winds as magnetic field lines from the two stars are forced together and reconnect (Jardine, Allen & Pollock 1996). Reconnection can occur either as a quasi-steady, or as an explosive process. The energy released is transferred into thermal energy through direct Joule heating of the plasma, into the kinetic energy of macroscopic motions, and into accelerated particles. Unfortunately, the role of magnetic reconnection in accelerating particles is highly complex, not least because of the many different types of reconnection, and the intricate magnetic environment that is usually associated with reconnection. This environment can accelerate particles directly (through strong electric fields), stochastically (i.e. through the second-order Fermi process due to high turbulence), and at the MHD shock waves which are an integral part of a reconnecting field (i.e. through DSA - see Priest & Forbes 2000, and references therein).

A rough upper limit of the power available for particle acceleration due to reconnection can be estimated. If reconnection occurs as a quasi-steady process, the power released in a current sheet of area A is

$$P \approx \frac{\pi}{4 \ln R_m} \frac{B^2}{8\pi} v_A A, \quad (1)$$

where R_m is the magnetic Reynold’s number, B is the magnetic field strength, and v_A is the Alfvén speed (Petschek 1964). In a CWB system like WR 140, the area of the current sheet, A , is approximately the area of the apex of the WCR i.e. $A \sim \pi r_O^2$, where r_O is the distance from the stagnation point of the WCR to the centre of the O star. For our model B (see Table 1), $R_m \sim 10^{20}$, $A \sim 5 \times 10^{27}$ cm², $v_A \approx 6 \times 10^7$ cm s⁻¹, and $B = 1.2$ G, so $P \sim 3 \times 10^{32}$ erg s⁻¹. While P is strongly dependent on B , and could therefore be considerably higher than this estimate, only some fraction of this total power will end up in non-thermal particles. Conversely, the maximum power that is available to DSA is the wind kinetic luminosity that is processed through the WCR ($\sim 10^{36}$ erg s⁻¹ in model B), and if only 1 per cent is placed into non-thermal particles, it should still dominate over the power available from reconnection. Therefore, we conclude that DSA appears to be more efficient at accelerating particles than reconnection (see also Bednarek 2005), and for the remainder of this work we assume that the non-thermal particles (electrons and ions) are created by DSA at the global shocks bounding the WCR. We ignore an additional (though likely small) contribution to the non-thermal radio emission from particles accelerated at wind-embedded shocks caused by the line-deshadowing instability in radiatively driven winds, since in WR 140 the non-thermal emission is clearly related to binarity.

A key property of DSA is the production of a power-law energy distribution of non-thermal particles i.e. $n(\gamma) \propto \gamma^{-p}$, where γ is the Lorentz factor (a discussion on this assumption can be found in Pittard et al. 2006). The maximum value of γ for electrons is obtained by balancing the rate of

energy increase from DSA to the rate of energy loss by IC cooling (e.g., see Eq. 8 in Pittard et al. 2006). While this is spatially dependent, and will also depend on orbital phase for binaries with eccentric orbits like WR 140, for simplicity throughout this work it is assumed that $\gamma_{\max} = 10^5$. For convenience, it is also assumed that $\gamma_{\max} = 10^5$ for the non-thermal ions (see Sec. 3.3 for further details).

The sonic Mach number of the stellar winds prior to the WCR is typically several hundred, so the shocks here are strong. In the test particle limit, the standard jump conditions for a strong shock apply, and $p = 2$. Variation from $p = 2$ can occur in a number of ways. For instance, when particle acceleration is efficient, the diffusion of non-thermal particles upstream of the subshock exerts a significant back-pressure on the pre-shock flow, causing the gas velocity to decrease prior to the subshock in a smooth precursor (Fig. 1 – based on fig. 1 in Berezhko & Ellison 1999). The velocity jump across the subshock in this situation is much less than in the classical shock, which results in a reduced post-shock thermal temperature. This process is known as “shock modification”. As the highest energy particles are able to diffuse further upstream from the subshock, and see the greatest velocity difference between the upstream and downstream flow, a concave curvature in the non-thermal particle energy spectrum is created (see Fig. 1). It is believed that the non-thermal ions are primarily responsible for modifying shocks because they are thought to dominate the non-thermal energy density, and the scale length of the precursor is set by their maximum energy. In contrast, the non-thermal electrons are largely confined to a region close to the subshock, as the diffusion length of electrons is much smaller than ions for a given Lorentz factor. Only those electrons with momenta $\gtrsim m_p c$ (i.e. with Lorentz factors $\gtrsim 2000$) are able to diffuse far enough upstream to see the required large velocity difference to obtain $p < 2$ (see fig. 1 in Ellison, Decourchelle & Ballet 2004). In CWB systems, the synchrotron emission at GHz frequencies is from electrons with relatively low momentum, where $p > 2$ is expected. At the apex of the WCR in model B, for example, electrons with $\gamma = 50$ (i.e. momentum $p = 50 m_e c \approx 0.03 m_p c$) produce synchrotron emission which peaks at $\nu = 0.29\nu_c \approx 3.6$ GHz (ν_c is specified in Eq. 5 of Dougherty et al. 2003).

Alternatively, acceleration at a sequence of shocks with energy losses between shocks (i.e. “re-acceleration”) can produce a spectral index which is flatter than that produced by a single shock. After an arbitrarily large number of shocks, $p = 1$ (independent of their strength - see Pope & Melrose 1994, and references therein). It is important to realize that shock modification and particle re-acceleration are not necessarily mutually exclusive. While $p > 2$ rules out re-acceleration and instead implies shock modification (or low Mach number shocks where $p > 2$ in the test particle limit), $p < 2$ can only be explained by re-acceleration (although the ion distribution in the shock vicinity may nevertheless have enough pressure to modify the shock structure). Finally, we note that some previous works claim that $p < 2$ can be obtained if the shock is oblique (i.e. the B-field is at some angle to the shock normal, Kirk & Heavens 1989; Naito & Takahara 1995). As these rely on a non-standard shock acceleration model, such as non-isotropic scattering, we do not consider this mechanism further.

Given the above possibilities, we set p as a free param-

eter for our model fits to the observed radio emission. Regardless of the exact form of the non-thermal particle spectrum immediately post-shock, as the particles advect downstream IC cooling modifies the energy distribution of non-thermal electrons, and p becomes dependent on both their spatial position and γ (Pittard et al. 2006).

Since the B-field and the population of non-thermal particles are not determined from first principles in these models, the magnetic energy density U_B and the non-thermal electron energy density $U_{\text{rel},e}$ are assumed to be proportional to the thermal particle internal energy density, U_{th} , by way of the constants ζ_B and $\zeta_{\text{rel},e}$ i.e. $U_B = \zeta_B U_{\text{th}}$, and $U_{\text{rel},e} = \zeta_{\text{rel},e} U_{\text{th}}$. Compared to other work where the B-field is assumed to be spatially invariant, this approximation has the benefit that the B-field declines away from the symmetry axis. We assume that the post-shock B-field is highly tangled, as in our earlier work. Because the accelerated particles, in wind-embedded shocks and the WCR, can amplify the background B-field (Bell 2004), while reconnection reduces the magnetic field, one cannot simply determine the B-field in the WCR from assumptions about the strength of the surface magnetic field at each star. We note that direct evidence for magnetic field amplification has recently been obtained for SN 1006 (Berezhko, Ksenofontov & Völk 2003; Ellison & Cassam-Chenaï 2005) and Cas A (Berezhko & Völk 2004).

When modelling the radio emission from specific systems, ζ_B and $\zeta_{\text{rel},e}$ are chosen to best match the observed radio emission. As ζ_B decreases, the value of $\zeta_{\text{rel},e}$ required to reproduce an observed radio flux increases. A lower limit on ζ_B can be obtained from the fact that the Razin turnover frequency, ν_R , increases with declining ζ_B ($\nu_R \approx 20n_e/B$, where n_e is the electron number density and the magnetic field, $B = \sqrt{8\pi U_B}$), or because the value of $\zeta_{\text{rel},e}$ required to match an observed flux may become uncomfortably large. An upper limit on ζ_B is obtained from the necessary conditions for particle acceleration (see Eichler & Usov 1993). Since there is currently little guidance for the ratio of $\zeta_B/\zeta_{\text{rel},e}$ in CWB systems, we consider this to be a free parameter in our models, subject to the above constraints.

At this stage, we make no allowance for the possibility that the shock obliquity has a strong influence on the *normalization* of the non-thermal electron energy density. However, we note that in general, the higher the obliquity, the lower the injection efficiency, although particles are actually accelerated more rapidly as a result of shock drift along the surface and slower diffusion in the shock normal direction (e.g., Ellison, Baring & Jones 1995, 1996; Ellison, Jones & Baring 1999). In wide binaries, such as WR 140, the shocks near the head of the WCR may be highly oblique. While this perhaps indicates that the acceleration efficiencies should be fairly low, the picture is further complicated if the level of magnetic turbulence is at the Bohm limit, since then the shock does not have a well-defined obliquity, and strong cross-field diffusion results in efficient injection (see fig. 6 in Ellison, Baring & Jones 1995). Such concerns are beyond the scope of the present work.

The thermal radio emission is also dependent on the degree of clumping within the winds. There is now considerable observational evidence that the winds of massive stars are clumpy (e.g., Crowther et al. 2002; Hillier et al. 2003; Massa et al. 2003; Repolust et al. 2004;

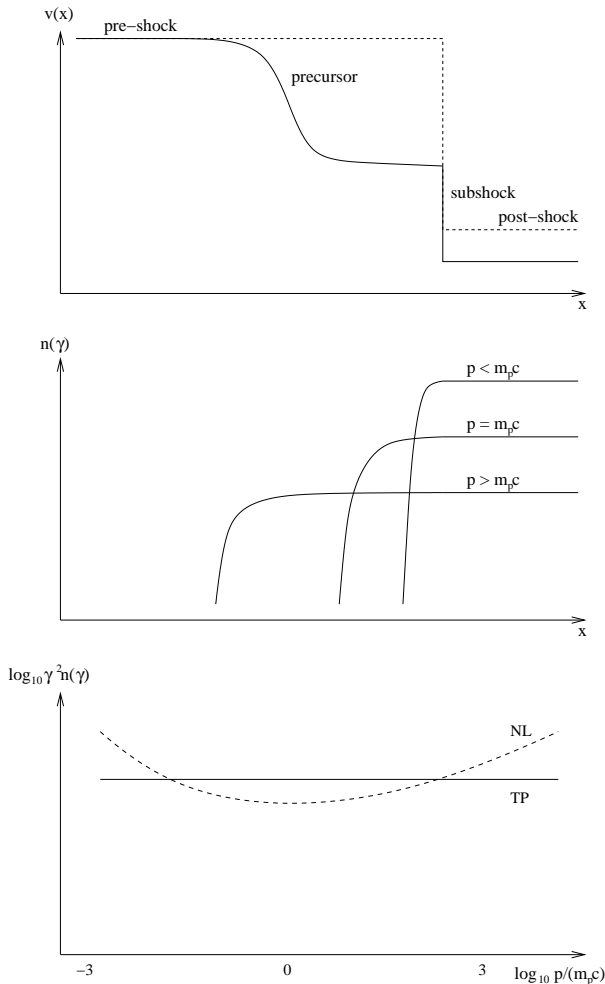


Figure 1. Top: Schematic structure of a strong shock. If DSA places a negligible amount of energy into accelerated particles, an ordinary discontinuous classical shock occurs (dashed line). In this case the undisturbed pre-shock flow is separated from the post-shock flow by a discontinuity known as a subshock across which the flow velocity decreases, and the density and pressure increase. The scale length of the subshock, l_s , is determined by microphysical dissipation processes that result in gas heating. In contrast, when particle acceleration is efficient, the diffusion of non-thermal particles upstream of the subshock exerts a back-pressure on the pre-shock flow, causing the gas velocity to decrease prior to the subshock in a smooth precursor (solid line). The scale length of the precursor, l_d ($\gg l_s$), is approximately the diffusion length of the highest energy particles. Middle: The spatial distribution of the number density of non-thermal particles as a function of energy in the modified shock. The highest energy particles are able to diffuse further upstream from the subshock, and see the greatest velocity difference between the upstream and downstream flow. Non-thermal particles in the precursor are typically scattered back across the subshock, and either undergo further acceleration, or escape downstream. Bottom: The non-thermal particle energy spectrum, multiplied by γ^2 to emphasize the spectral curvature of the non-linear (i.e. efficient particle acceleration) case. When DSA places relatively little energy into accelerated particles the standard test particle spectrum is obtained (solid). In contrast, the modified shock produced when DSA is efficient leads to a concave curvature in the non-thermal particle energy spectrum (dashed - see Ellison, Decourchelle & Ballet 2004, and references therein).

Fullerton, Massa & Prinja 2005; Owocki & Cohen 2006). Simple arguments suggest that in wide binaries where the WCR is largely adiabatic, clumps are rapidly destroyed upon encountering the WCR (Pittard et al. 2006). Therefore, in the following models we assume that the unshocked winds are clumpy (with the same degree of clumping for both winds), and the WCR smooth (see also Sec. 4.2.4). Additional details relating to the hydrodynamical code, and the method and assumptions used to obtain the various emission and absorption coefficients in each cell, can be found in Pittard et al. (2006) and references therein.

3 NON-THERMAL X-RAY AND γ -RAY EMISSION

The presence of non-thermal electrons and ions should also give rise to X-ray and γ -ray emission from several separate mechanisms, including IC scattering, relativistic bremsstrahlung, and pion decay (the non-thermal electrons are not energetic enough to produce synchrotron X-ray emission). While definitive evidence for non-thermal X-ray and γ -ray emission from CWBs does not yet exist, many of the yet unidentified EGRET sources appear correlated with populations of massive stars (Romero, Benaglia & Torres 1999), and some systems appear to show a power-law tail extending to higher energies than the thermal X-ray emission (Viotti et al. 2004; De Becker et al. 2004b). A critical question is whether the non-thermal X-ray and γ -ray fluxes from CWB systems are sufficiently high to be detected with instruments onboard current observatories, and instruments on observatories that will be operational in the near future.

Previous predictions of the IC emission have been typically based on the fact that the ratio of the luminosity from IC scattering to the synchrotron luminosity is equal to the ratio of the photon energy density, U_{ph} , to the magnetic field energy density, U_B :

$$\frac{L_{ic}}{L_{sync}} = \frac{U_{ph}}{U_B}. \quad (2)$$

Typically, the ratio of U_{ph}/U_B is evaluated only at the stagnation point, whereas in reality the emission is generated throughout the WCR, with U_{ph}/U_B varying spatially. In addition, L_{sync} is usually set to the *observed* synchrotron luminosity, whereas free-free absorption by the extended wind envelopes can be significant (see, e.g., Pittard et al. 2006). In such cases the intrinsic synchrotron luminosity, and consequently the non-thermal X-ray and γ -ray luminosity, are underestimated. Furthermore, the predictive power of Eq. 2 is greatly undermined by the fact that the magnetic field strength in the WCR is generally not known with any certainty. Since $U_B \propto B^2$, small changes in the estimated value of the magnetic field strength, B , can lead to large changes in L_{ic} (see fig. 3 in Benaglia & Romero 2003).

To obtain a more robust estimate of the IC emission from CWB systems, the population and spatial distribution of non-thermal electrons must be directly determined. This information can, in principle, be acquired from model fits to radio data, since the IC emission arises from the same non-thermal electrons responsible for the synchrotron radio emission. As already noted, an improved theoretical basis for the modelling of the radio emission from such systems

was developed by Dougherty et al. (2003) and Pittard et al. (2006), and we use this as the foundation for our calculations of the non-thermal X-ray and γ -ray emission. Key benefits over previous work include a more realistic description of the geometry of the WCR, the self-consistent evolution of the energy distribution of the non-thermal electrons as they advect downstream from their acceleration site, and absorption of high energy photons by pair production in the stellar radiation fields. Our predictions for the expected γ -ray emission are based on model fits to the available radio and X-ray data, which allow us to constrain the range of free parameters and build in a degree of consistency for our estimates.

3.1 IC emission

IC cooling is a major energy loss mechanism for non-thermal electrons in CWB systems, and the non-thermal X-ray and γ -ray luminosity should exceed the synchrotron radio luminosity by several orders of magnitude. In the Thomson regime, the average energy of a photon after isotropic IC scattering is (Blumenthal & Gould 1970)

$$h\nu_{\text{IC}} \sim \frac{4}{3} \gamma^2 h\nu_*. \quad (3)$$

Since the average photon energy of an early-type star, $h\nu_* \sim 10$ eV, Lorentz factors of order $10 - 10^4$ are sufficient to produce IC X-ray and γ -ray radiation. The resulting emission has a spectral shape which is identical to the intrinsic synchrotron emission at radio frequencies. For our calculations, we assume that the scattering is isotropic and takes place in the Thomson limit. While a more thorough treatment would take account of Klein-Nishina effects, which are important at high energies, recent work has shown that the resulting change to the non-thermal electron energy distribution is rather small when the stellar separation is $\gtrsim 2 \times 10^{14}$ cm (Reimer, Pohl & Reimer 2005). This condition is satisfied in WR 140 between orbital phases $\phi = 0.1 - 0.9$, and also in wider binaries like WR 146 and WR 147.

Consideration should also be given to the anisotropic nature of the IC process, where the emitted power is dependent on the scattering angle. However, if the O star is in front of the WR star (which is the case for WR 140 at $\phi = 0.837$ - see Sec. 4), the variation in the resulting emission is less than a factor of 2.5 (Reimer, Pohl & Reimer 2005). In Sec. 4.3.2, we show that the other uncertainties affecting the IC emission, such as the value of ζ_e determined from fitting the radio data, are at least comparable in magnitude, so we leave this issue to future work.

3.2 Relativistic Bremsstrahlung

Bremsstrahlung radiation is produced when a charged particle is accelerated in the Coulomb field of another charged particle. It is possible to obtain emission at γ -ray energies if one of the particles is relativistic, since photons of comparable energy to that of the emitting particle can be produced. Inverse bremsstrahlung, produced by collisions between high energy ions and thermal electrons, is an insignificant contribution to the total emission unless the ratio of the energy density of non-thermal ions to electrons is very high. Therefore, we concentrate on emission produced by collisions between non-thermal electrons and thermal electrons and ions.

A more detailed discussion can be found in Baring et al. (1999).

The rate of photon production in the energy interval between ϵ_γ and $\epsilon_\gamma + d\epsilon_\gamma$ by an electron of kinetic energy E_e is

$$\frac{dn_\gamma(E_e, \epsilon_\gamma)}{dt} = v_e \left[n_e \sigma_{ee}(E_e, \epsilon_\gamma) + \sum_i n_i Z_i^2 \sigma_{ep}(E_e, \epsilon_\gamma) \right], \quad (4)$$

where ϵ_γ is the photon energy in units of $m_e c^2$, v_e is the relative velocity of the colliding particles, n_i and n_e are the number density of ions and electrons respectively, and Z_i is the charge of the ion. The electron-proton cross section, σ_{ep} , is the Bethe-Heitler cross section evaluated in the Born approximation. We determine σ_{ep} for any electron energy, relativistic or non-relativistic, using equation 3BN in Koch & Motz (1959), and omit the Coulomb corrections at low energies. The cross section for electron collisions with fully ionized ions has a Z^2 charge dependence, accounting for the factor in Eq. 4. For the electron-electron cross section, σ_{ee} , the approach noted in Baring et al. (1999) is followed.

For $\gamma_e \gg 1$ and $\epsilon_\gamma \gg 1$, the cross sections depend only on the particle's charge and not its mass, so $\sigma_{ep} = \sigma_{ee}$. The ratio of the electron-electron to electron-ion contributions is then simply

$$\frac{n_e}{\sum_i Z_i^2 n_i}. \quad (5)$$

For material with solar abundances this ratio is ≈ 0.86 , while in the shocked WR wind of WR 140 it is ≈ 0.47 (see Sec. 4). At high energies, the bremsstrahlung spectrum (in units of photons $\text{s}^{-1} \text{cm}^{-2}$) has a spectral index which reflects that of the non-thermal particles i.e. p .

3.3 π^0 decay

High energy hadronic collisions can create neutral pions which subsequently decay into two γ -ray photons, e.g., $p + p \rightarrow \pi^0 + X$, $\pi^0 \rightarrow \gamma + \gamma$. The final stage has a branching ratio of ≈ 98.8 per cent (the decay $\pi^0 \rightarrow \gamma + e^+ + e^-$ accounts for the other 1.2 per cent). The pion decay process yields information on the population of non-thermal nucleons, in contrast to the IC and bremsstrahlung processes where the emission is dependent on the population of non-thermal electrons. Therefore, an estimate of the γ -ray flux from the decay of neutral pions requires knowledge of the energy density of the relativistic ions, though it is reasonably certain that DSA transfers considerably less energy into non-thermal electrons than into non-thermal ions (e.g., Baring et al. 1999). The relative difficulty of accelerating electrons is also consistent with the well established value for the ratio of proton to electron energy densities for Galactic cosmic rays of ~ 100 (Longair 1994). Therefore, it is assumed that $\zeta_{\text{rel},i} = 100\zeta_{\text{rel},e}$, unless otherwise noted.

The cross-section for hadronic collisions depends on the ionic species involved, so we first consider the π^0 emissivity from proton-proton collisions. The production rate for neutral pions of energy E_π per thermal proton can be easily evaluated using a δ -functional approximation for the differential cross-section (Aharonian & Atoyan 1996):

$$q_\pi(E_\pi) = \int \delta(E_\pi - f_\pi E_k) \sigma_{pp2}(E) J(E) dE, \quad (6)$$

where E_k is the kinetic energy of the non-thermal protons, f_π is the fraction of the kinetic energy of the non-thermal proton which is transferred to the π^0 meson, and $J(E)$ is the flux of non-thermal protons of total energy E (protons $\text{s}^{-1} \text{cm}^{-2} \text{GeV}^{-1}$). Here, only the contribution to the γ -ray emission from the leading pion is considered. After the interaction the non-thermal proton keeps approximately half of its energy, while the other half goes to pions. On average the leading pion gets approximately one third of this energy, or approximately one sixth of the energy of the non-thermal proton, so $f_\pi = 0.17$. $\sigma_{\text{pp}2}$ is the total inelastic cross section (Aharonian & Atoyan 1996). Thus, Eq. 6 becomes (pions $\text{s}^{-1} \text{GeV}^{-1} \text{H}^{-1}$):

$$q_\pi(E_\pi) = \frac{1}{f_\pi} \sigma_{\text{pp}2}(E) J(E). \quad (7)$$

The γ -ray emissivity (photons $\text{s}^{-1} \text{GeV}^{-1} \text{H}^{-1}$) is then

$$q_\gamma(E_\gamma) = 2 \int_{E_{\min}}^{\infty} \frac{q_\pi(E_\pi)}{\sqrt{E_\pi^2 - m_\pi^2 c^4}} dE_\pi, \quad (8)$$

where $E_{\min} = E_\gamma + m_\pi^2 c^4 / 4E_\gamma$ and m_π is the mass of the neutral pion (134.9766 MeV/ c^2).

In CWB systems, we must account for the composition of non-thermal and thermal ions. For collisions involving two nuclei with atomic weights A_1 and A_2 , the cross section is (Orth & Buffington 1976)

$$\sigma \sim (A_1^{3/8} + A_2^{3/8} - 1)^2 \sigma_{\text{pp}2}. \quad (9)$$

This prescription is appropriate for proton-helium interactions, but its validity for heavy nuclei, such as Fe, is unclear. It is adopted here since its potential inaccuracy is small compared to the other uncertainties and assumptions in this work. In the case of WR stars, such as WR 140, the wind contains little or no hydrogen, and the cross-section for pion decay is best calculated relative to the He-He cross section $\sigma_{\alpha\alpha} = 5.6\sigma_{\text{pp}2}$.

The thermal abundances are those of the winds, but determination of the non-thermal abundances is not so straightforward. In the simplest test-particle calculations of DSA i.e. with no feedback, all particles accelerated in a given shock will have identical power-law spectral shapes in momentum, regardless of their charge, and the non-thermal particle composition reflects the composition of thermal particles. However, in non-linear models, the spectral shape and injection and acceleration efficiencies are dependent on the ionic species. Ions with large mass-to-charge (A/Q) ratios diffuse further upstream than protons of the same energy per nucleon (provided that both are non-relativistic), and are accelerated more efficiently and obtain a flatter spectrum because they “see” a larger velocity difference and are more easily injected to suprathermal energies. Among the volatile elements, observational support comes from Galactic cosmic rays, which show an enhancement of heavier elements relative to lighter ones (Meyer, Drury & Ellison 1997). A general enhancement of the refractory elements relative to the volatile ones is also apparent from the Galactic cosmic ray composition (Meyer, Drury & Ellison 1997). This has been explained by acceleration of dust grains (which can have huge mass-to-charge ratios of $\sim 10^4 - 10^8$), followed by the sputtering of atoms from these grains. However, the harsh UV radiation fields in CWB systems means that it is unlikely that dust grains can form near the head

of the WCR, so an enhancement of refractory elements is not expected (while several CWB systems, including WR 140, show observational signatures of either episodic or continuous dust formation (e.g., Williams 1996; Tuthill et al. 1999; Marchenko et al. 2002), in all cases the dust is thought to form well downstream of the apex of the WCR). Observations have further revealed that the relative abundance of heavy ions increases with energy (see Bykov & Toptygin 2001; Hillas 2005). This is supported by the results from non-linear models where variation with shock speed and Mach number is also seen (Ellison, Drury & Meyer 1997). Finally, it is also possible that shock obliquity may influence the non-thermal particle composition.

Given these uncertainties, we adopt the following simplifications: i) identical spectra for all non-thermal particles, ii) identical composition to that of the thermal particles, iii) no dependence on the shock obliquity. Considering only protons and Helium nuclei, an enhancement to the pion production rate in Eq. 7 of 1.61 is obtained for material of solar composition. Greater enhancements are obtained for the nuclear processed material in WR winds. For example, if collisions involving He, C, O and Ne are considered for the WC7 wind abundances in WR 140 (see Sec. 4.2.1), then $\sigma \sim 1.4\sigma_{\alpha\alpha} \sim 7.8\sigma_{\text{pp}2}$.

In CWB systems, the maximum energy of non-thermal electrons is set by the balance between the rate of energy gain from DSA, and the rate of energy loss from IC cooling. As the latter is ineffective for ions, the maximum non-thermal ion energy is instead set by geometrical considerations. The diffusion length scale $l_d = \kappa/v_{\text{shk}}$, where $\kappa = \lambda v/3$ is the spatial diffusion coefficient, v_{shk} is the shock speed, v is the particle speed, and $\lambda \approx 3r_g$ is the mean free path (Eichler & Usov 1993). For highly relativistic protons, the maximum particle gyroradius $r_g = \gamma_{\max} m_p c^2 / eB$. We can equate l_d to the approximate radius of curvature of the shocks i.e. $l_d \sim r_O$, where r_O is the distance between the stagnation point in the WCR and the O star. Our preferred fits to the radio data of WR 140 in Sec. 2 yield B-fields which imply that for ions $\gamma_{\max} \sim 2 \times 10^4 - 2 \times 10^5$. For convenience, we adopt $\gamma_{\max} = 10^5$ i.e. the same as for the electrons, for the remainder of this work (for ions, $\gamma_{\max} \propto DB$, but as it is not yet known how the magnetic field in the WCR varies with the stellar separation, D , γ_{\max} may increase or decrease with D). We also adopt the same spectral index for the non-thermal ions as for the immediately post-shock non-thermal electrons. The spectral index of the electrons can be significantly modified in the downstream flow due to IC cooling, whereas IC cooling is insignificant for non-thermal ions and they maintain a power-law energy distribution as they advect away from the shocks.

3.4 γ -ray absorption

γ -rays above a suitable threshold energy may create electron-positron pairs via interaction with a lower energy photon or with charged nuclei. While the latter process has an insignificant optical depth in CWB systems, in contrast the high stellar radiation energy density may be a significant source of opacity to high energy γ -rays. The probability of absorption depends on the cosine of the angle between the directions of the two photons, μ . For a high energy photon

of energy E_γ interacting with a stellar photon of energy ϵ , the optical depth is given by

$$\frac{d\tau}{dr} = \int \sigma(\chi)(1-\mu)n(\epsilon, \mu, r)d\epsilon d\mu, \quad (10)$$

where $\chi = \sqrt{E_\gamma \epsilon (1-\mu)/2}$ is the centre-of-momentum frame energy¹ scaled by $m_e c^2$,

$$\sigma(\chi) = \frac{\pi r_e^2}{\chi^6} \left[(2\chi^4 + 2\chi^2 - 1) \ln(\chi + \sqrt{\chi^2 - 1}) - \chi(1 + \chi^2)\sqrt{\chi^2 - 1} \right], \quad (11)$$

where $r_e = e^2/m_e c^2$, and $n(\epsilon, \mu, r)$ is the number density of stellar photons. The threshold for pair production, and thus for absorption, is $\chi \geq 1$.

In wide CWBs it can be assumed that the stars are point-like, and that the stellar photons stream radially away from each star. This allows the $(1-\mu)$ term to be taken out of the integral in Eq. 10. The optical depth as a function of non-thermal photon energy from the stagnation point to an observer for two models of WR 140 is shown in Fig. 2. Table 1 summarizes some key parameters of these models.

Of the two models shown in Fig. 2, both the shock apex and the line of sight from the apex are closer to the O star in model B. The greatest opacity occurs at ~ 100 GeV, where optical depths as high as ~ 25 (model B) may be reached. At lower and higher energies the optical depth decreases, and optical depth unity occurs at approximately 50 GeV and 5 TeV for model A, and at approximately 20 GeV and 40 TeV for model B. In practice, the effective optical depth is likely to be somewhat smaller due to the spatial extension of the emission region. More accurate calculations using radiative transfer along multiple sight lines are presented in Sec. 4.4. The CWB system WR 146, which has a wider stellar separation, is expected to have a maximum optical depth to pair-production of ~ 1 . In WR 147, which is wider still, the attenuation is negligible. Similar conclusions have also been noted by Reimer, Pohl & Reimer (2005).

4 NON-THERMAL EMISSION MODELS OF WR 140

In this section we apply our model to WR 140 (HD 193793), the archetype of long-period CWB systems. WR 140 consists of a WC7 star and an O4–5 star in a highly elliptical orbit ($e \approx 0.88$), and is well known for the dramatic variations in its emission from near-IR to radio wavelengths (Williams et al. 1990; White & Becker 1995), and also at X-ray energies (Zhekov & Skinner 2000; Pollock, Corcoran & Stevens 2002; Pollock et al. 2005), during its 7.9-year orbital period. The variability appears to be linked to the WCR, which experiences significant changes as the stellar separation varies between ~ 2 AU at periastron and ~ 30 AU at apastron. The observed radio emission increases by up to two orders of magnitude between periastron and a frequency-dependent peak between orbital phases 0.65 to 0.85, followed by a steep decline. The decline of the radio emission prior to periastron is consistent with

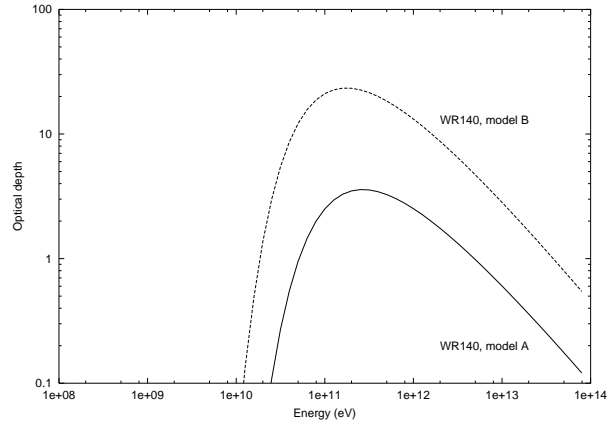


Figure 2. The optical depth from two-photon pair production as a function of the non-thermal photon energy for a single line-of-sight from the stagnation point of the WCR in WR 140. The shape of the curves reflects the Planck distribution for the stellar photons. We show calculations at $\phi = 0.837$ for models A and B (see Sec. 4). In each case, only the photons from the O star are considered. The energy of peak absorption is a function of the viewing angle, θ , and increases as θ decreases.

the extinction suffered by the X-ray emission at these orbital phases. A tantalizing clue that the shocks in WR 140 might be modified comes from the observation that the X-ray lightcurve does not follow the expected $1/D$ variation for an adiabatic WCR (Pollock, Corcoran & Stevens 2002). This may hint that a substantial amount of energy is being placed into accelerated particles, with the efficiency varying as a function of phase. Another possibility is that the WCR becomes radiative near periastron, leading to the reduced variation seen (Varriacatt, Williams & Ashok 2004).

WR 140 is also notable for its possible association with an EGRET source, lying on the outskirts of the positional error box of 3EG J2022+4317 (Romero, Benaglia & Torres 1999). While the error box has a radius of $\approx 0.7^\circ$, WR 140 is the only known high-energy source in the vicinity. 3EG J2022+4317 has a flux of $(24.7 \pm 5.2) \times 10^{-8}$ photons $\text{s}^{-1} \text{cm}^{-2}$, a photon spectral index $\Gamma = 2.31 \pm 0.19$ (where $N(E) \propto E^{-\Gamma}$), and is formally non-variable (Benaglia & Romero 2003). However, given that it was only detected in 3 observing periods (at approximate orbital phases 0.97, 1.00, and 1.16), the upper limits may hide real variability.

It has been suggested previously that better agreement may be obtained between observed and modelled radio lightcurves if the wind of the WR star is disc-like (White & Becker 1995), but a specific (and unusual) orientation is required for consistency with polarization measurements (see Marchenko et al. 2003, and discussion therein), and there is no evidence for such a disk in X-ray observations (Pollock, Corcoran & Stevens 2002). In the following, it is assumed that the undisturbed wind is isotropic.

4.1 Details of the hydrodynamical model

The assumption of axisymmetry in our 2D models is good until orbital phases of ~ 0.97 , as the orbital eccentricity is so high. Since radiative braking (Gayley, Owocki & Cranmer

¹ The equation for χ contains a typo in Baring & Harding (1997).

1997) or inhibition (Stevens & Pollock 1994) is not expected to be important, the wind speeds are assumed to be constant. The calculations are performed on a grid with 1600×800 cells, which spans the range $0 \leq r \leq 4 \times 10^{15}$ cm, $-4 \times 10^{15} \leq z \leq 4 \times 10^{15}$ cm, and is large enough to capture the vast majority of the radio and X-ray emission from the WCR, though inevitably the models underestimate the radio flux at the lowest frequencies considered.

4.2 Parameters of WR 140

Recent high-resolution VLBA observations at 8.4 GHz between orbital phase 0.7 and 0.9 have provided important new constraints to models of WR 140 (Dougherty et al. 2005). An arc of emission is observed, resembling the bow-shaped morphology expected for the WCR, and rotates as the orbit progresses. This rotation allows derivation of the orbit inclination and semi-major axis, leading to a geometric distance determination (1.85 ± 0.16 kpc) that is independent of stellar parameters. This distance is greater than previously thought, and implies the O star is a supergiant. Therefore, we adopt $\log(L_{\text{bol}}/L_{\odot}) = 6.18$ and $v_{\infty} = 3100 \text{ km s}^{-1}$ for the O4–5I primary, and $\log(L_{\text{bol}}/L_{\odot}) = 5.5$ and $v_{\infty} = 2860 \text{ km s}^{-1}$ for the WC7 secondary (Dougherty et al. 2005). These luminosities are higher than average for the spectral types. Herrero, Puls & Najarro (2002) and Repolust et al. (2004) suggest a typical value of 5.7–5.9 for an O4–5 supergiant, while the mean luminosity for WC7 stars is about 0.4 dex lower (although the scatter in the absolute magnitude of WC7s is ~ 1 magnitude). Therefore, there may be some scope for lowering the adopted luminosities.

Dougherty et al. (2005) used the models of Zhekov & Skinner (2000) of the observed thermal X-ray luminosity to derive a mass-loss rate for the WR star of $4.3 \times 10^{-5} M_{\odot} \text{ yr}^{-1}$. However, there are several complicating factors, such as the inadequately constrained composition of the WC7 wind. Also, models of the thermal X-ray emission typically assume unmodified, collisional shocks, whereas collisionless shocks are expected in wide CWBs like WR 140. Lastly, the X-ray luminosity is dependent on η . As η increases, the opening angle of the WCR increases and the greater the fraction of the WC7 wind that will be shocked. These issues are explored in the following sub-sections, leading to improved estimates of the mass-loss rates and η in WR 140.

4.2.1 WR wind composition

The thermal X-ray emission is largely from the shocked WR star wind (Pittard & Stevens 2002). Hence, it is particularly sensitive to the abundance of He and C since the free electrons are largely stripped from these elements. For a pure He and C wind, the continuum flux scales as $(2^2 + (\text{C}/\text{He})6^2)$, where C/He is the ratio of abundance by number of C and He (Pollock et al. 2005). Unfortunately, the mass fraction of C in WC stars spans the range 0.2 – 0.6, with no strong sensitivity with spectral type. In this work, we assume that C/He = 0.25 by number ($X(\text{C}) = 0.4$ by mass), as the ratio of C IV 5471/He II 5411 is comparable to that in WR 90 (Dessart et al. 2000, P. Crowther, priv. communication). We

Table 1. Some key parameters for our models of WR 140 at $\phi = 0.837$ (Sec. 4). D is the binary separation, η is the wind momentum ratio, and d is the distance of the system. U_{th} , U_{B} , U_{ph} , n_{e} , and B are all evaluated at the stagnation point, while the pre-shock Alfvénic Mach number, M_{A} , is evaluated immediately upstream of the WR shock on the line of centers, assuming that at this point the shock is highly perpendicular and that the B-field is compressed by a factor of 4. We provide two values for n_{e} - these are for the WR and O star side of the contact discontinuity respectively. θ is the angle of the line of sight into the system, and is measured from the line perpendicular to the line of centers of the two stars: $\theta = +90^\circ$ corresponds to the O star in front of the WR star, $\theta = 0^\circ$ corresponds to quadrature, and $\theta = -90^\circ$ corresponds to the WR star in front of the O star.

Parameter	Model A	Model B
D (10^{14} cm)		3.13
$\log(L_{\text{O,bol}}/L_{\odot})$		6.18
$\log(L_{\text{WR,bol}}/L_{\odot})$		5.5
d (kpc)		1.85
η	0.22	0.02
$\zeta_{\text{rel,e}}$	1.38×10^{-3}	5.36×10^{-3}
ζ_{B}	0.05	0.05
U_{th} (erg cm^{-3})	0.78	1.2
U_{B} (erg cm^{-3})	0.04	0.06
U_{ph} (erg cm^{-3})	1.6	10.3
n_{e} (WR) (cm^{-3})	3.7×10^6	6.0×10^6
n_{e} (OB) (cm^{-3})	1.3×10^7	2.0×10^7
B (mG)	990	1200
M_{A}	11.4	11.9
θ	5°	35°

note that Eenens & Williams (1992) had previously measured $\text{C}/\text{He} = 0.15$ for WR 140. The O abundance in WC stars is also poorly constrained, though the number ratio of O/He is estimated as 0.03 ± 0.01 for WR 90 (WC7) and WR 135 (WC8) (Dessart et al. 2000). Since Hillier & Miller (1999) had earlier obtained O/He=0.1 for WR 111 (WC5), we adopt O/He = 0.05 ($X(\text{O}) = 0.1$). Our values for C/He and O/He lie within the range considered by Pollock et al. (2005), while we note that in comparison Zhekov & Skinner (2000) adopt C and O abundances which are below the lower end of the ranges noted above. With these assumptions, the mass fractions for the WC7 wind are $X = 0.0$, $Y = 0.5$, $Z = 0.5$. Solar abundances are assumed for the O star (mass fractions $X = 0.705$, $Y = 0.275$, $Z = 0.020$). Both winds are assumed to have a temperature of 10,000 K, with an ionization structure of H^+ , He^+ , and CNO^{2+} .

4.2.2 Collisionless shocks - electron thermalization and shock modification

Previous models of the X-ray emission from the WCR in wide CWB systems have usually assumed that the shocks are collisional with immediate equilibration of the post-shock electron and ion temperatures, though in reality they are collisionless (e.g., Draine & McKee 1993). While Zhekov & Skinner (2000) and Pollock et al. (2005) examined the possibility that $T_{\text{e}} \lesssim T_{\text{i}}$, shock modification has yet to be considered.

In collisionless shocks, there is growing observational evidence that the ratio of post-shock electron to ion

temperature, T_e/T_i , is a function of the shock speed (e.g., Rakowski 2005). Temperature equilibration through Coulomb collisions and plasma instabilities then occurs some distance downstream. In the context of WR 140, the correlation of X-ray line widths with ionization potential indicates that the post-shock plasma has yet to reach ionization equilibrium (Pollock et al. 2005). Line-profile models which assume rapid ionization equilibrium (Henley, Stevens & Pittard 2003) are unable to reproduce the observed correlation (Henley 2005). Since the timescale for energy transfer from ions to electrons is of the same order as the ionization timescale, the observed soft X-ray continuum emission can be accounted for naturally (Pollock et al. 2005). However, the physics of the heating process in the shock layer remains poorly understood, and shocks which are efficient at accelerating particles may equilibrate their electron and ion thermal populations much faster, in addition to reducing the equilibrium value of T_e and T_i (Ellison, Decourchelle & Ballet 2004). In this case, the X-ray spectrum is softened due to the reduction in the post-shock electron temperature behind a weaker subshock (see Fig. 1). Therefore, in WR 140, the low value of T_e may result from shock modification acting in tandem with slow post-shock equilibration. A simple calculation reveals that the non-thermal particles in the precursor have a negligible effect on the ionization of the pre-shock gas, which is consistent with the observed lack of line emission near the wind terminal speeds (Pollock et al. 2005).

A full understanding of WR 140's spectrum requires a detailed hydrodynamical model which accounts for the large post-shock equilibration timescales of the plasma ionization and electron and ion temperatures, combined with the acceleration of non-thermal particles and their effect on the shocks bounding the WCR and both the upstream and downstream flow (e.g., Pollock et al. 2005). As the development of such models is not trivial, here the synthetic X-ray spectra are calculated from models of unmodified collisional shocks. Given this simplification and the uncertainties described above, we adopt a rather pragmatic approach, and concentrate on obtaining a comparable flux at ~ 3 keV. Absorption is negligible at this energy at the chosen phase (see Fig. 18) for reasonable viewing angles, while at higher energies the relative softness of the observed emission is clear evidence for either $T_e < T_i$, or shock modification (see Fig. 4).

The fact that the thermal X-ray luminosity from the WCR, L_x , scales as \dot{M}^2 when the post-shock gas is largely adiabatic means that even if shock modification leads to fairly substantial (e.g., factor of two) changes in L_x , mass-loss rates derived from models with unmodified shocks will be much less affected. Moreover, the inferred mass-loss rates are largely insensitive to the assumption of $T_e = T_i$. For instance, setting $T_e = 0.5T_i$ throughout the entire WCR reduces the emission at 3 keV by 23 per cent compared to a model with $T_e = T_i$. An increase of only 14 per cent in the mass-loss rates is required for the original flux to be regained. In this way we can still obtain useful estimates of the stellar mass-loss rates for the modelling work which follows.

4.2.3 WR mass-loss rate from thermal X-ray models

Having specified the composition of the winds (Sec. 4.2.1) and unmodified, collisional shocks (Sec. 4.2.2), theoretical calculations of the X-ray emission, based on axisymmetric 2D simulations of the stellar winds and the WCR, can now be made. The X-ray emissivity is calculated using the MEKAL emission code (Mewe, Kaastra & Liedahl 1995, and references therein) for optically thin thermal plasma, and ionization equilibrium and rapid thermalization of the electrons is assumed.

The intrinsic (i.e. prior to any absorption) X-ray emission calculated from a model of the WCR with a fixed WC7 mass-loss rate, but for two different values of η , is shown in Fig. 3. As η increases, the X-ray flux increases, as explained earlier. Clearly, in order that the X-ray flux calculated from hydrodynamical models of the WCR is comparable to observations, the mass-loss rate of the WC7 star must be adjusted as η is varied.

There have been a number of X-ray observations of WR 140 in recent years, and we choose to use an ASCA observation taken on Dec. 20 1999 ($\phi = 0.837$). At this phase the X-ray luminosity is climbing rapidly (Pollock, Corcoran & Stevens 2002), while the radio emission is around its maximum intensity, and the stellar separation, ($D = 3.13 \times 10^{14}$ cm, see Dougherty et al. 2005), is sufficiently large that the shocked gas in the WCR is approximately adiabatic, allowing easy adjustment of the model mass-loss rates in order to obtain a specific X-ray flux. The mass-loss rates required to match the observed X-ray emission at $\phi = 0.837$, as a function of η , are noted in Table 2. Fig. 4 demonstrates that the X-ray emission from two of these models is comparable to the observed emission at ~ 3 keV, as required. Models of the radio emission (Sec. 4.3.2) indicate η is likely to have a value near the lower end of the range covered by Table 2. This implies the mass-loss rate of the O4–5 supergiant in WR 140 is lower ($\approx 8 \times 10^{-7} M_\odot \text{ yr}^{-1}$) than the suggested values in Repolust et al. (2004) ($8.6 - 8.8 \times 10^{-6} M_\odot \text{ yr}^{-1}$). However, an order of magnitude reduction in the mass-loss rate is consistent with the recent estimates of Fullerton, Massa & Prinja (2005).

We note that Pollock et al. (2005) determine $\dot{M}_{\text{WR}} \sim 1.5 \times 10^{-5} M_\odot \text{ yr}^{-1}$ from the degree of circumstellar absorption observed by Chandra near periastron. While this value is independent of the clumping in the winds, it is likely to be a lower limit since the overall absorption of emission from the WCR is probably somewhat less than occurs for emission near the apex of the WCR. This method will also underestimate \dot{M}_{WR} if there are regions of O star wind between the observer and the WR star at this phase due to the curvature of the WCR induced by the orbital motion of the stars. Therefore, it is argued that the range of values of \dot{M}_{WR} considered in our models is consistent with this constraint (see Table 2), and does not preclude values of η as low as 0.02.

Due to the relatively low abundance of C and O assumed by Zhekov & Skinner (2000), their derived mass-loss rates for $\eta = 0.0353$ are higher than ours (cf. their model A and AA), even though the system distance has since been revised upwards. We also note that the wind parameters noted in Dougherty et al. (2005) overpredict the observed X-ray emission by a factor of about 8, although

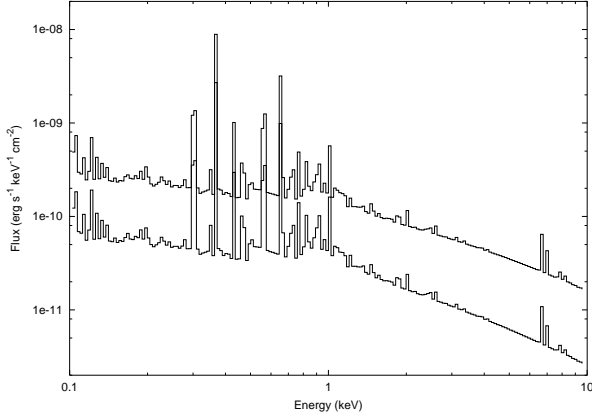


Figure 3. Comparison of the intrinsic thermal X-ray emission calculated from hydrodynamical models of the WCR in WR 140 at $\phi = 0.837$ for two different values of η , assuming unmodified collisional shocks (Sec. 4.2.2). $\eta = 0.22$ (top) and $\eta = 0.0353$ (bottom). In these calculations the mass-loss rate of the WC7 star and the terminal wind speeds were fixed ($\dot{M}_{\text{WR}} = 4.3 \times 10^{-5} M_{\odot} \text{ yr}^{-1}$, $v_{\infty, \text{WR}} = 2860 \text{ km s}^{-1}$, $v_{\infty, \text{O}} = 3100 \text{ km s}^{-1}$), while the mass-loss rate of the O star was varied according to the desired value of η . The continuum flux is also sensitive to the adopted abundance of the WR wind (see Sec. 4.2.1).

Table 2. The mass-loss rates (in units of $10^{-6} M_{\odot} \text{ yr}^{-1}$) required to match the observed X-ray flux at 3 keV and $\phi = 0.837$ as a function of η . Column 4 indicates lower limits for the volume filling factor, f , of clumps in the winds, as determined from a comparison between the X-ray and radio derived mass-loss rates (Sec. 4.2.4). For simplicity, we assume that the two winds have the same values of f . Recent analyses of O star winds indicate that $f \sim 0.02 - 0.1$ (see Fullerton, Massa & Prinja 2005, and references therein). Columns 5-7 note approximate values of θ (see caption of Table 1 for a definition of θ) for which the sight lines are parallel to the asymptotic opening angles of the WR shock, contact discontinuity, and O shock.

η	\dot{M}_{WR}	\dot{M}_{O}	f	θ_{WR}	θ_{CD}	θ_{O}
0.02	43.3	0.80	0.199	41°	59°	90°
0.0353	33.3	1.09	0.118	35°	54°	79°
0.055	27.2	1.38	0.079	30°	49°	71°
0.0825	23.2	1.76	0.057	25°	42°	65°
0.11	20.2	2.05	0.043	19°	38°	56°
0.16	17.2	2.54	0.031	11°	32°	52°
0.22	14.9	3.02	0.024	4°	27°	48°

Reimer, Pohl & Reimer (2005) have recently based work on these values.

Given the existing uncertainties with respect to the degree of shock modification, and the amount of post-shock electron heating and the timescale for electron and ion temperatures to reach equilibrium, Fig. 4 demonstrates that it is difficult to uniquely determine the WR star mass-loss rate and η from the X-ray spectrum alone. While a simpler, and perhaps a more reliable, method of determining η in CWB systems with highly eccentric orbits involves utilizing the duration of any X-ray “eclipse” (see, e.g., Pittard & Corcoran 2002), the very short eclipse seen in the lightcurve of WR 140

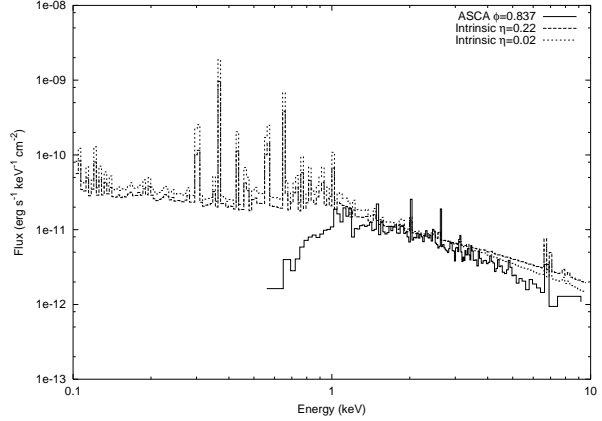


Figure 4. The intrinsic thermal X-ray emission from hydrodynamical models of the WCR at orbital phase $\phi = 0.837$ with $\eta = 0.22$ (dashed) and $\eta = 0.02$ (dotted). There is a slight decrease in the hardness of the model spectra with η , as expected. Also shown is the observed X-ray emission (solid). The X-ray emission from the models (at 3 keV) is comparable to the observed emission, though the latter is softer. As discussed in Sec. 4.2.2, this indicates that either $T_e < T_i$, or that the sub-shock is weakened as a result of efficient particle acceleration.

(Pollock et al. 2005) means that a detailed analysis using 3D hydrodynamical simulations is probably needed. Therefore, we turn to the high quality radio spectra now available to further constrain η (Sec. 4.3.2).

4.2.4 Wind clumping

As we have mentioned previously, there is now a great deal of observational evidence for clumping in the winds of early-type stars, and additional support is provided by models of radiatively-driven winds. The degree of clumping is parameterized by a volume filling factor, f , where it is assumed that the clumps occupy a fraction f of the wind volume, with the interclump medium being of negligible density. Radio-derived mass-loss rates of clumpy winds are related to those of smooth winds by $\dot{M} = \dot{M}_{\text{smooth}}/f^{1/2}$, since the thermal flux S_{ff} and the radius of the $\tau = 1$ surface $R_{\tau=1}$ increase accordingly (e.g., see Eqs. 16 and 17 from Pittard et al. 2006). This relationship is necessarily more complicated in binaries, where the degree of clumping may be different for each wind, and where the thermal emission from the WCR may make a non-negligible contribution to the total thermal emission (see Fig. 11 in Pittard et al. 2006). Bearing this in mind, we proceed by assuming the WR wind dominates the thermal radio emission in WR 140, so that a value for f can be deduced from a comparison of the X-ray and radio derived mass-loss rates. The unclumped estimate of $5.3 \times 10^{-5} M_{\odot} \text{ yr}^{-1}$ from Williams et al. (1990) translates into $9.7 \times 10^{-5} M_{\odot} \text{ yr}^{-1}$ for a system distance of 1.85 kpc, and leads to the lower limits for f noted in Table 2. The mass-loss rate of Williams et al. (1990) assumes the radio flux at $\phi = 0.0$ is entirely thermal, which is far from clear. While such assumptions should be avoided if at all possible, our approach is very conservative in the sense that the theoretical thermal flux from the unshocked winds cannot exceed the measured flux at periastron. Since the total observed flux

at $\phi = 0.837$ is $\sim 20\times$ greater at 5 GHz and $\sim 5\times$ greater at 22 GHz than our estimate of the thermal flux, the models in Sec. 4.3.2 should not be overly sensitive to our choice of f , although p will be overestimated slightly if the thermal flux is in fact lower than assumed. Wind clumping also affects the radius of the $\tau = 1$ surface. In the clumpy WR wind in our models, $R_{\tau=1}$ has values of 8.8, 4.0, and 1.8×10^{14} cm at 1.6, 5, and 15 GHz. This is independent of the variation in \dot{M}_{WR} with η due to the corresponding variation in f . As mentioned previously (Sec. 2), we assume that both winds have equal amounts of clumping (i.e. the same value of f), and that the shocked gas in the WCR is smooth.

4.3 Models of the radio data

We concentrate on obtaining reasonable spectral fits to the radio data at the same orbital phase ($\phi = 0.837$) we determined potential values for stellar mass-loss rates and corresponding values of η from the observed X-ray emission (see Sec. 4.2.3). The brightness temperature of the radio emission is $\approx 3 \times 10^7$ K at this phase, so the observed emission is dominated by non-thermal processes (Dougherty et al. 2005). Therefore, a good estimate of the population of relativistic electrons can be obtained from models at this phase, permitting a search for signatures of shock modification and particle re-acceleration, and predictions for non-thermal X-ray and γ -ray emission. We will apply our modelling to a variety of orbital phases in a forthcoming paper.

There are several free parameters used to fit the observed radio emission, including η , the index of the non-thermal electron energy distribution, p , and $\zeta_{\text{rel,e}}$ and ζ_{B} , which normalize the model spectra and the magnetic field strength (and hence the impact of the Razin effect). The effect of reducing the luminosity of the stars is also investigated. The line of sight angle into the system at $\phi = 0.837$ is specified by the orbit derivation of Dougherty et al. (2005) as $\theta = 52^\circ$, though the uncertainty in this value is large ($\sim 10^\circ$) and we allow θ to vary substantially ($\pm 10 - 20^\circ$) in our models. A clear signature of shock modification will arise if $p > 2$ is required to fit the radio data, while $p < 2$ implies particle re-acceleration (although shock modification may still occur, as noted in Sec. 2).

4.3.1 Parameter study

Before attempting a fit to the $\phi = 0.837$ data, it is instructive to examine how the model spectra vary with θ , η , p , ζ_{B} , and L_{bol} . Fig. 5 shows how the model *synchrotron* spectra change as θ is varied, for models with $\eta = 0.11$, $p = 2.0$, $\zeta_{\text{rel,e}} = 0.215$, and $\zeta_{\text{B}} = 2.6 \times 10^{-4}$. The Razin effect produces a turnover at about 2.3 GHz, while the high frequency emission from each model tends to the same slope as the free-free attenuation becomes negligible. The sensitivity of the spectrum at low frequencies to changes in θ is expected since the size of the radio photosphere is larger than the stellar separation. At high frequencies the radio photosphere is smaller and has a commensurately weaker influence on the absorption of emission from the WCR. The synchrotron emission is least affected by free-free absorption when $\theta \approx 20^\circ$ (i.e. when the lines of sight are roughly parallel to the asymptotic angle of the WR shock), and the turnover

frequency is the same as that of the intrinsic synchrotron emission. A dramatic increase in the level of free-free absorption occurs as θ decreases and the WR wind moves in front of the WCR, with maximum absorption at $\theta = -90^\circ$ (i.e. WR star in front). For $\theta \lesssim 20^\circ$, free-free absorption causes the low frequency turnover. As the line of sight swings through the WCR from the WR shock to the O shock i.e. $\theta = 20 \rightarrow 56^\circ$, the level of absorption again increases, although in a somewhat complicated fashion as the source is extended and there are multiple lines of sight. While free-free absorption determines the slope of the spectrum between 3 and 20–30 GHz, it is only between 50° and 60° , when the sight lines move out of the WCR and into the O wind, that the turnover due to free-free absorption dominates over the Razin frequency, and the turnover becomes very broad. The turnover frequency increases as the O wind moves in front of the WCR i.e. as $\theta \rightarrow 90^\circ$. The smaller stellar separation in the models presented here results in free-free absorption having an influence to much higher frequencies than in the models shown in Fig. 10 of Dougherty et al. (2003).

It is interesting to note that when the sight lines are through the WCR, a turndown or “kink” is visible in the spectrum at a few 10’s of GHz (this is most clearly seen when $\theta = 50^\circ$). Typically, such turndowns are attributed to a change in the non-thermal energy spectrum. However, it is certainly not the cause here, because the intrinsic synchrotron spectrum does not display such a kink (although spectral breaks from IC cooling occur in our models, the break frequency is spatially dependent, and is smoothed out once the flux is integrated over the entire WCR - see fig. 3 in Pittard et al. 2006). It is clear that lines of sight to the WCR are optically thin at frequencies above 20–30 GHz, and almost all, if not all, the synchrotron emission from the WCR is seen.

The variation of the spectra as a function of η is shown in Fig. 6, where the total emission (synchrotron plus free-free) is displayed. In this and the following figures, emission between 0.5 and 50 GHz is examined, since this is approximately the frequency range of the observations. The spectral variations in Fig. 6 bear some resemblance to the changes with θ , since as η varies, the relative angle of the sight lines to the WCR changes if θ is fixed. For $\eta = 0.055 - 0.16$, the line of sight is through the lower opacity WCR. When $\eta = 0.22$, it is through the unshocked O star wind, and the synchrotron emission from the WCR suffers more free-free absorption than seen in the other models, which results in the low frequency turnover occurring at a higher frequency (c.f. Fig. 5). For the remaining models, the reduced level of free-free absorption means that the turnover is the result of the Razin effect, and therefore occurs at approximately the same frequency in each case (since ζ_{B} is fixed). It is clear from Fig. 6 that the spectral slope between 10–40 GHz steepens as η decreases (the slight upward curvature in the $\eta = 0.055$ model near 40 GHz is caused by rising free-free emission), which is due to the change in the relative angle of the sight lines with respect to the WCR, as seen in Fig. 5, and the resulting change in the free-free opacity. While Fig. 6 does not show frequencies as high as Fig. 5, the synchrotron emission tends to a similar slope in all models (since p is the same in each model) with a slight steepening as η decreases due to the WCR moving closer towards the O star, and the amount of IC cooling increasing.

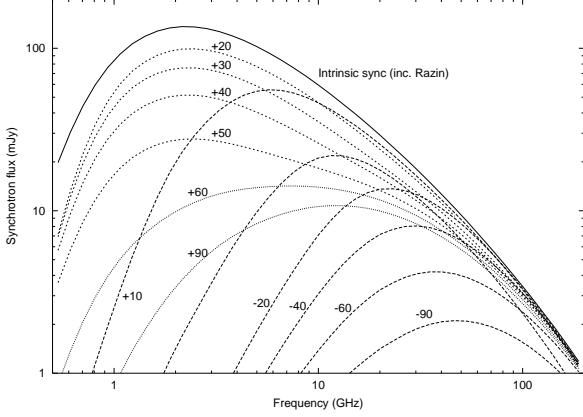


Figure 5. The influence of θ on the observed *synchrotron* emission. All models have $\eta = 0.11$, $p = 2.0$, $\zeta_{\text{rel,e}} = 0.215$, and $\zeta_B = 2.6 \times 10^{-4}$. The lines of sight are through the WR wind when $-90^\circ < \theta \lesssim 19^\circ$, through the WCR when $19^\circ \lesssim \theta \lesssim 56^\circ$, and through the O wind when $56^\circ \lesssim \theta < 90^\circ$, as indicated by the long-dashed, short-dashed, and dotted lines respectively (see Table 2). The intrinsic synchrotron emission is indicated by the solid line.

Fig. 7 shows the effect of varying the slope of the non-thermal electron energy distribution. As p decreases, the slope of the intrinsic synchrotron emission increases (if IC cooling is negligible, $S_\nu \propto \nu^\alpha$, and the spectral index is given by $\alpha = (1 - p)/2$), resulting in flatter attenuated spectra.

Fig. 8 illustrates the effect of changing ζ_B . As ζ_B is reduced, the spectral index above 4 GHz increases. By decreasing ζ_B (and thus B), the synchrotron emission at a given frequency arises from non-thermal electrons with higher Lorentz factors ($\nu \propto \gamma^2 B$), and thus sample a steeper slope for the non-thermal electron energy distribution due to the increased impact of IC cooling at high γ (see fig. 3 in Pittard et al. 2006). At very low values of ζ_B , the Razin effect becomes the dominant mechanism responsible for the low frequency turnover in Fig. 8.

The effect of adjusting the stellar luminosities is shown in Fig. 9. For simplicity, the luminosity of both stars is adjusted by the same amount, although the amount of IC cooling is primarily determined by the luminosity of the O supergiant. As the L_{bol} values are reduced, the impact of IC cooling decreases, and the synchrotron emission becomes less steep. Clearly a specific spectral slope can be obtained with a larger value of p if the model values of L_{bol} are reduced. As we shall see in Sec. 4.3.2, this may imply that re-acceleration need not be so strong (i.e. fewer shocks needed). For a given energy density of non-thermal electrons immediately post-shock, a reduction in IC cooling also produces an increase in the overall flux. It is conceivable that the assumptions in Sec. 4.2 may overestimate the stellar luminosities, but with one exception the models in the rest of this work are based on the luminosities noted in Table 1.

4.3.2 Spectral fits at $\phi = 0.837$

Our initial aim was to determine parameter values directly from model fits to the radio data. Unfortunately, reasonable fits to the data are possible with a range of parameters. For

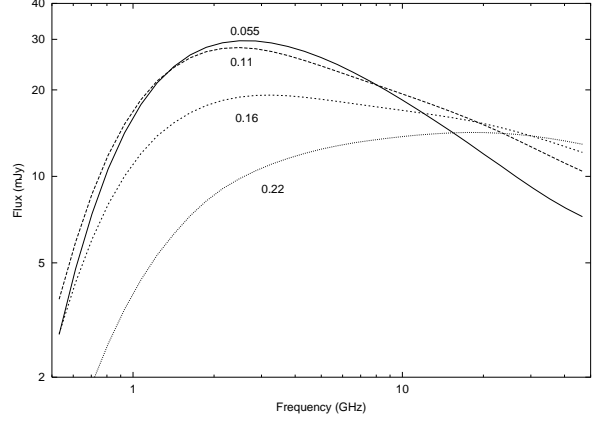


Figure 6. The influence of η on the model radio spectra. IC cooling and the Razin effect are included in these calculations. Ionic cooling and synchrotron self-absorption are negligible. All models have $\theta = 50^\circ$, $p = 2.0$, $\zeta_{\text{rel,e}} = 0.215$, and $\zeta_B = 2.6 \times 10^{-4}$, though the mass-loss rates and f were varied according to Table 2. The line of sight is through the WCR in all models except for $\eta = 0.22$, when it is through the unshocked O star wind. The synchrotron emission from the WCR dominates the free-free emission from the winds and WCR for the chosen parameters.

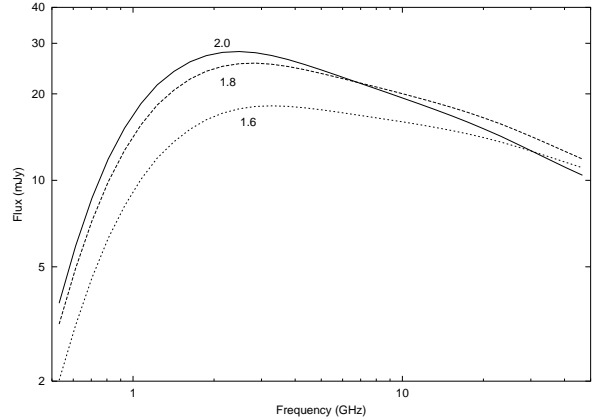


Figure 7. The influence of p on the model radio spectra. All models have $\eta = 0.11$, $\theta = 50^\circ$, $\zeta_{\text{rel,e}} = 0.215$, and $\zeta_B = 2.6 \times 10^{-4}$, and the line of sight is through the WCR.

example, by varying p and θ similar fits are attained over a wide range of η . Furthermore, the data can be fit with either free-free absorption or the Razin effect responsible for the low frequency turnover. However, despite this degeneracy of models, it is possible to discriminate between models by using other properties, such as the values of θ and $\zeta_{\text{rel,i}}$ required by each model, which we discuss later in this section. Parameters for a variety of model fits are listed in Table 3.

Two model fits are shown in Fig. 10 where free-free absorption is the cause of the low frequency turnover. For both of the models in Fig. 10, $\zeta_B = 0.05$ was assumed. With this restriction, $p = 1.4$ is needed to match the slope of the data points between 5 and 22 GHz. For free-free absorption to be sufficiently large that the model spectrum passes through the 1.5 GHz datapoint, the lines of sight into the system must pass through the unshocked WR wind: such fits can-

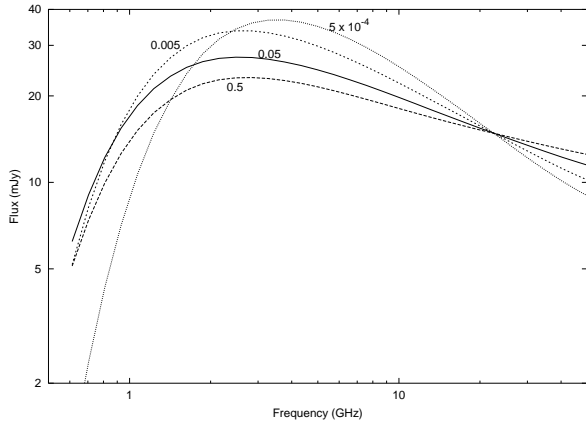


Figure 8. The influence of ζ_B on the model radio spectra. All models have $\eta = 0.0353$, $p = 1.4$, and $\theta = 27^\circ$, and the line of sight is through the unshocked WR wind. $\zeta_{\text{rel,e}}$ was adjusted in each model to obtain a specific flux at 22 GHz.

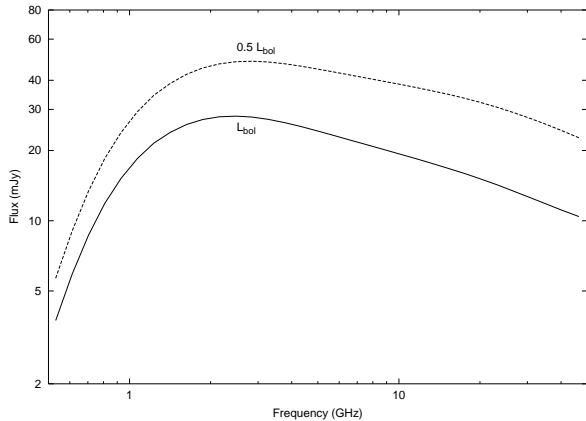


Figure 9. The influence of the stellar luminosities on the model radio spectra. Both models had $\eta = 0.11$, $p = 2.0$, $\zeta_{\text{rel,e}} = 0.215$, $\zeta_B = 2.6 \times 10^{-4}$, and $\theta = 50^\circ$, and the line of sight is through the WCR.

not be obtained when the sightlines are through the WCR because the free-free absorption is too low, while sightlines through the unshocked O wind require $p \gtrsim 2.5$ for the non-thermal electron distribution to offset the synchrotron spectrum between 5–22 GHz becoming flatter as $\theta \rightarrow 90^\circ$ and the free-free opacity increases (cf. Fig. 5). Such values of p require a compression ratio of ≈ 3 which would be appropriate for an MHD shock with appreciable magnetic pressure. As we do not expect the magnetic field to be high enough in WR 140 to affect the dynamics of the WCR we discard this possibility.

Since the opening angle of the WCR varies with η , the value of θ required to match the low frequency synchrotron turnover varies in a similar fashion. For the models in Fig. 10, θ is 5° for model A and 35° for model B (acceptable fits with η between 0.02 and 0.22 can also be obtained). The value of θ from model A is inconsistent with the 52° determined by Dougherty et al. (2005) at this phase, and while in model B it is still different by some considerable margin, it is not entirely implausible given the large uncertainty that

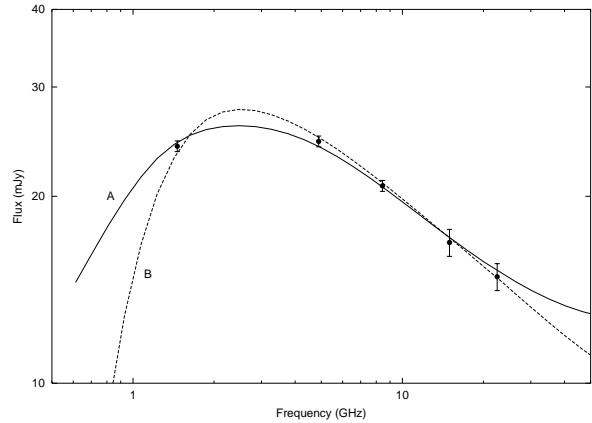


Figure 10. Model fits to radio data of WR 140 at $\phi = 0.837$. In these models the low frequency turnover is due to free-free absorption. The data are represented by solid circles; in this and subsequent figures we assume that the uncertainty in the absolute flux scale is 5 per cent for $\nu \geq 15$ GHz and 2 per cent for $\nu < 15$ GHz (Perley & Taylor 2003). The model parameters are noted in Table 3, and the line of sight is through the unshocked WR wind. Model A has a shallower low frequency turnover and a concave curvature to the high frequency total emission. The variation of the high frequency emission is due to differences in the slope of the synchrotron and free-free emission in both models. The thermal flux from the unshocked winds and the WCR is ≈ 4 mJy at 50 GHz in both models.

exists for θ . It is anticipated that models with $\eta < 0.02$ should result in fits with θ closer to the value determined by Dougherty et al. (2005), but η is not expected to be lower than ~ 0.01 because the mass-loss rate of the WR star then becomes too large.

The slope of the high frequency synchrotron emission is sensitive to both p (Fig. 7) and ζ_B (Fig. 8). Since there is almost complete degeneracy between these parameters, a variety of fits with different families of p and ζ_B can be obtained (Fig. 11). For a given η , the value of θ required to match the low frequency turnover is largely unchanged in these fits. If the stellar luminosity is reduced, fits with a higher value of p can be obtained, as shown in Fig. 12. However, we are unable to fit the data with $\eta = 0.02$ and $p = 2$, despite making the other parameters as favorable as possible for this task (e.g., $\zeta_B = 0.05$ and luminosities reduced by a factor of two). As already noted, we are also able to obtain reasonable fits to the data when the Razin effect is responsible for the low frequency turnover. Again fits of similar quality can be obtained across a wide range of η and p , as demonstrated in Fig. 13. In these models an attempt was made to match θ as closely as possible to the value determined from the orbital solution of Dougherty et al. (2005).

Before the relative merits of the models with either the Razin effect or free-free absorption being responsible for the low frequency turnover are considered, it is worth looking at the make-up of each of these models. The intrinsic synchrotron (i.e. before circumstellar absorption) and the free-free emission components to the total flux for model A where the low frequency turnover is due to free-free absorption are shown in Fig. 14. The free-free flux is negligible in comparison to the synchrotron flux, which only suffers significant absorption at low frequencies. In this case, the ob-

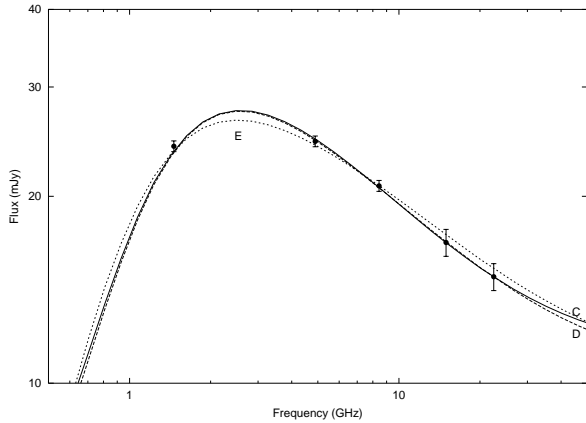


Figure 11. Model fits to the radio data at $\phi = 0.837$, again where the low frequency turnover is due to free-free absorption (models C, D, and E). Due to the sensitivity of the slope of the high frequency synchrotron emission to both p and ζ_B , it is possible to obtain, for a given η , fits of similar quality with different values of p and B . All models had $\eta = 0.11$ (see Table 3).

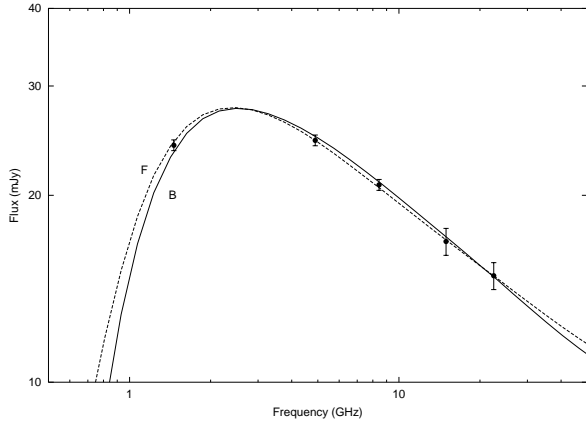


Figure 12. Models of the radio data at $\phi = 0.837$ which demonstrate that it is possible to obtain fits of similar quality with a higher value of p when the stellar luminosities are reduced. Both models (B and F) had $\eta = 0.02$ and $\zeta_B = 0.05$ (see Table 3).

served synchrotron luminosity between 1–40 GHz is roughly 90 per cent of the intrinsic synchrotron luminosity. Somewhat paradoxically, the intrinsic synchrotron emission from models where the low frequency turnover is caused by the Razin effect can experience more severe free-free absorption, as seen from a comparison of Figs. 14 and 15. This is because the free-free absorption is smallest when the sight lines are closely parallel to the WR shock (as is the case for model A), and is significantly greater when the sight lines are deeper within the WCR (e.g., compare the 10 GHz flux in Fig. 5 when $\theta = 10$ or 20° with the flux when $\theta = 40^\circ$ - see also the dotted curve in Fig. 12b in Pittard et al. 2006). The observed synchrotron luminosity in Fig. 15 is only 40 per cent of the intrinsic synchrotron luminosity, and in such cases the IC luminosity predicted using Eq. 2 will be substantially underestimated.

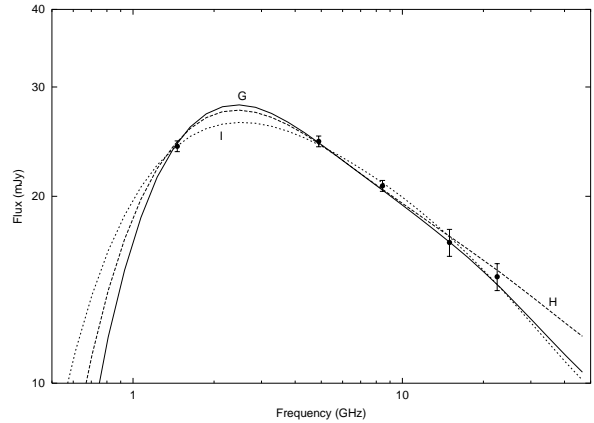


Figure 13. Model fits to the radio data at $\phi = 0.837$ where the low frequency turnover is due to the Razin effect (models G, H, and I). The model parameters are again noted in Table 3.

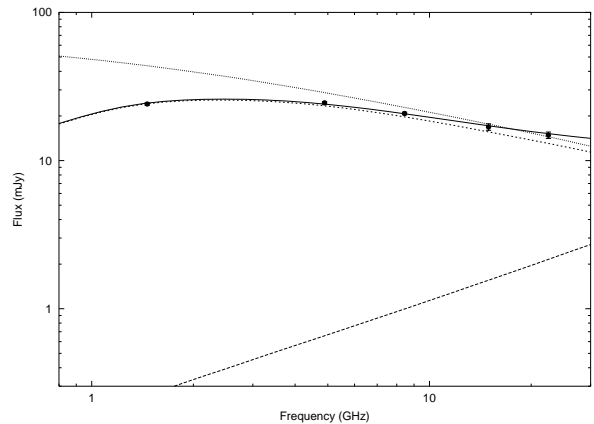


Figure 14. The amount of free-free absorption affecting the intrinsic synchrotron emission in model A, where the low frequency turnover is due to free-free absorption. Various emission components are shown - free-free flux (long-dashed), synchrotron flux (short-dashed), intrinsic synchrotron flux (dotted), and total flux (solid). The spectral index of the intrinsic synchrotron emission is -0.34 between 1.5 and 5 GHz, and steepens to -0.47 between 15 and 22.5 GHz. This illustrates the effect of IC cooling, since, for $p = 1.4$, $\alpha = -0.2$ is expected.

4.3.3 Synthetic radio images

The spatial distributions of radio emission from models A and B are shown in the left and right panels of Fig. 16. In all panels the intensity of emission from the WCR exceeds that from the stars, though the relative amount of free-free emission increases strongly with frequency. Model A is viewed at low inclination, while model B is viewed at a somewhat higher inclination (Table 3). The absorption of emission from the far side of the WCR by the O star wind is negligible in model A, but significant in model B, as evident by the dearth of emission near the O star. As expected, this hole is much larger at 1.7 GHz than at 8.4 GHz. The O star is not located at the centroid of the hole, since the O star wind is restricted by the WCR on the side facing the WR star, and those parts of the WCR with optically thin lines of sight

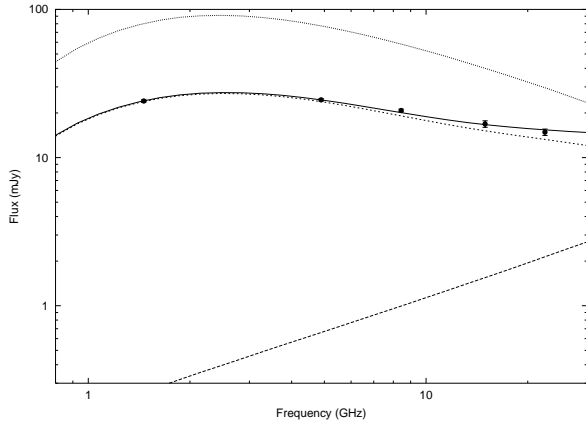


Figure 15. As Fig. 14 but for model J, where the Razin effect is responsible for the low frequency turnover.

Table 3. Parameters for model fits to the $\phi = 0.837$ radio data. In models A–F the low frequency turnover is due to free-free absorption, while in models G–J it is due to the Razin effect. The values of θ for which the sight lines are parallel to the asymptotic opening angle of the WR shock, contact discontinuity, and O shock are noted in Table 2.

Model	η	p	$\zeta_{\text{rel,e}}$	ζ_{B}	θ
A	0.22	1.4	1.38×10^{-3}	0.05	5°
B	0.02	1.4	5.36×10^{-3}	0.05	35°
C	0.11	1.53	2.26×10^{-4}	0.5	13°
D	0.11	1.4	2.03×10^{-3}	0.05	13°
E	0.11	1.1	2.79×10^{-2}	5.0×10^{-3}	14°
F	0.02	1.6	1.81×10^{-3}	0.05	40°
G	0.11	2.0	0.22	2.6×10^{-4}	50°
H	0.11	1.6	0.15	4.0×10^{-4}	44°
I	0.0353	1.4	0.14	1.0×10^{-3}	58°
J	0.22	1.5	0.14	4.0×10^{-4}	36°

through the outer envelope of the “modified” O star wind are predominantly observed. In addition, the intensity of the far side of the WCR is highest nearer the apex. The reduced opening angle of the WCR in model B relative to model A is clearly visible. IC cooling creates a “V”-shaped intensity distribution in model A, but this is not so clearly seen in model B, largely due to the difference in viewing angle.

Though not shown here, another important finding is that the relative position of the stars and the observed peak of the emission from the WCR is not necessarily related to η , due to the occultation of the WCR by the O star stellar wind. In fact, as θ increases and D decreases the absorption can become so large that the position of the WCR apex appears closer to the WR star than to the O star, despite the WR star having the stronger wind. Finally, we note that no offset between the centre of emission at 1.7 GHz and 8.4 GHz is seen, contrary to the report by Dougherty et al. (2005).

To more closely compare the model intensity distributions at 8.4 GHz to the VLBA images shown in Dougherty et al. (2005), we have used the AIPS subroutines UVCON to generate visibilities appropriate for a VLBA “observation” of our models. System noise estimates were

accounted for by including the performance characteristics of the VLBA telescopes, e.g., antenna efficiencies, system temperatures etc. The resulting visibilities were then imaged and deconvolved using the same procedure as used in Dougherty et al. (2005). The “simulated” observations shown in Fig. 17 illustrate that with perfect data it is possible to identify each model. However, when appropriate noise is added, this is not possible. We emphasize that the VLBA observations provide no information about the absorption in the system or the curvature of the WCR. Any curvature of the emission region, as a result of either the wind momentum ratio, or free-free absorption, is hidden once the models are convolved with the beam and noise is added.

4.3.4 Discussion of the radio models

In attempting to identify the most suitable models, it is noted that the fits in Fig. 13 require a low B-field within the WCR ($\zeta_{\text{B}} \sim 3 \times 10^{-4} - 10^{-3}$), which is far from equipartition with the energy density of non-thermal particles (electrons plus ions). Assuming a simple dipole field, this implies that the B-field at the surface of each star is very low, with little or no amplification in the WCR. As the synchrotron flux is proportional to $\zeta_{\text{rel,e}} \zeta_{\text{B}}^{3/4}$, large values of $\zeta_{\text{rel,e}}$ are required to normalize the model spectra to the data. The models (G–J) shown in Figs. 13 and 15 imply that 10–20 per cent of the available wind kinetic power processed through the shocks bounding the WCR (which is a small fraction of the total kinetic wind power in the system) is transferred to the non-thermal *electrons*. This is unacceptably high, and the available energy budget means that models G–J are inconsistent with $\zeta_{\text{rel,i}}/\zeta_{\text{rel,e}} \sim 100$. Hence, models where the low frequency turnover is due to free-free absorption are preferred. The high energy non-thermal emission from models G–J is also less consistent with current EGRET and INTEGRAL observations, and in model G the non-thermal X-ray flux exceeds the observed thermal flux. This is discussed further in Sec. 4.4.

Amongst models A–F, model E is notable for an extremely low value of p . The resulting high energy non-thermal spectrum is too flat if WR 140 is indeed associated with the EGRET source 3EG J2022+4317 (see Sec. 4.4.2). The magnetic energy density in model C is towards the high end of expectations, with $B = 3.3$ G at the apex of the WCR. A magnetic field this high is likely to prevent particle acceleration as the shock velocity does not exceed the phase velocity of whistler waves propagating normal to the shock (see Eichler & Usov 1993, for the necessary conditions). At this stage we also prefer to use the stellar luminosities determined in Dougherty et al. (2005), rather than reduced values such as used in model F, though further investigation of this matter is needed. On this basis, models A, B and D are preferred. Of these three models, the viewing angle of model B is closer to the value determined by Dougherty et al. (2005), and hence is the preferred model overall.

We now compare our estimate of η from model B to previous estimates. First, $\eta = 0.02$ is consistent with the value derived from Marchenko et al. (2003), from an analysis of the C III and He I line profiles around periastron. Dougherty et al. (2005) estimate a value an order of magnitude higher (0.22), but this is an indirect estimate based

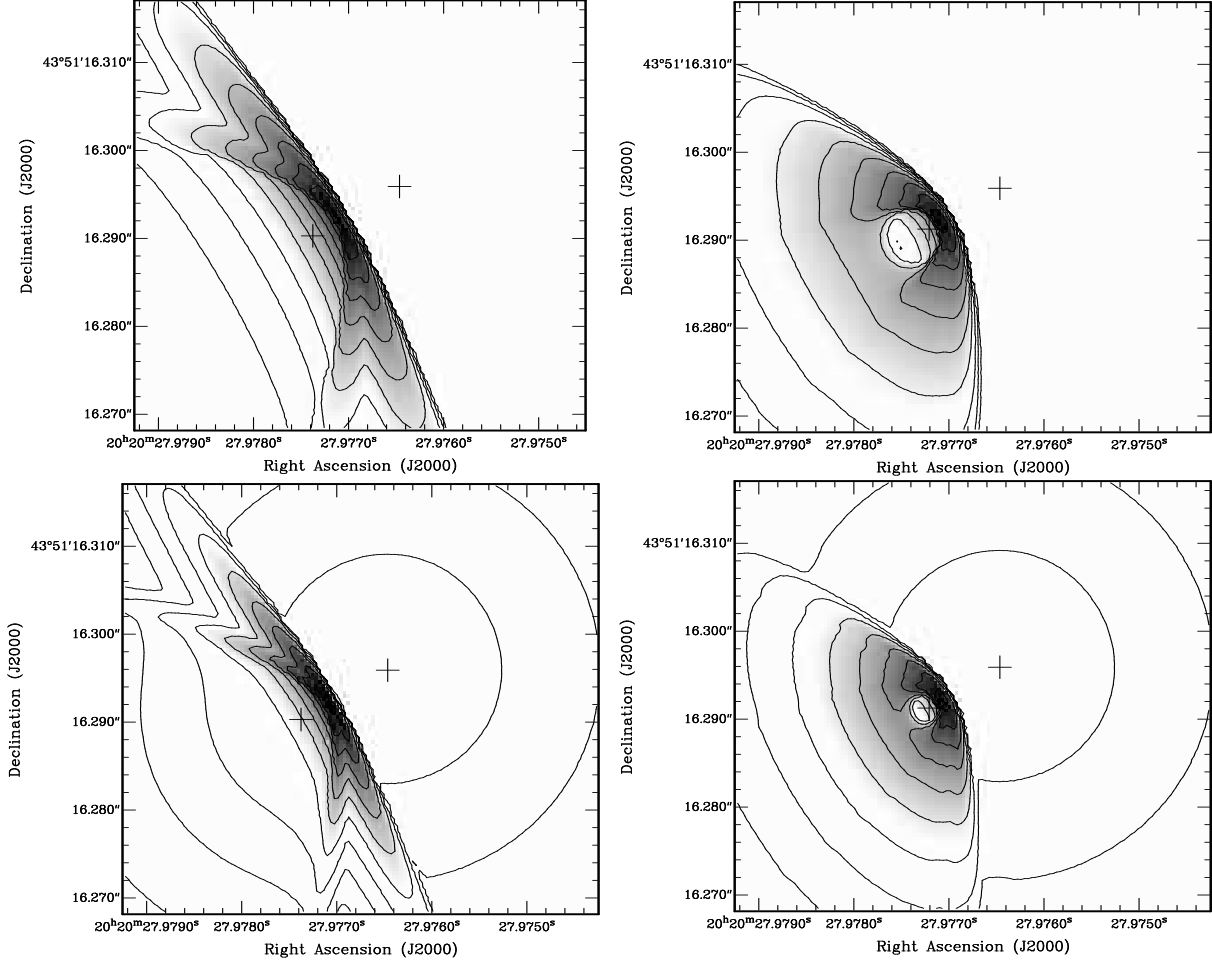


Figure 16. Intensity distributions at 1.7 GHz (top) and 8.4 GHz (bottom) from model A (left) and model B (right) of WR 140. The contour levels are spaced apart by 0.5 dex, are chosen to highlight the large-scale structure, and are identical in both model's at a specific frequency, though change with frequency. The positions of the stars are indicated by crosses (WR star to the upper-right of the O star). The effect of different wind momentum ratios and line of sight angles are clearly visible.

on an assumed mass-loss rate for the O supergiant. They argue that the angle is consistent with the opening angle of the WCR as estimated from the VLBA images. However, as shown in Fig. 17 (lower), our synthetic VLBA images show that at this orbital phase we should not expect the opening angle of the WCR to be constrained by the VLBA observations. Varricatt, Williams & Ashok (2004), from He I absorption in the WR wind, determine a lower limit to the half-opening angle of 42° , which is consistent with the value for the WR shock in model B.

4.4 The high energy emission

4.4.1 Models of the high energy emission

The parameters obtained from the models of the radio data in Sec. 4.3 allow prediction of the IC and relativistic bremsstrahlung flux, and by specifying the ratio of the energy density of electrons to ions it is possible to predict the flux from the decay of neutral pions. Such calculations can be used to further constrain the spectral index of the non-

thermal particles and thus the nature of their acceleration, as demonstrated in this section.

The non-thermal emission from model B is shown in Fig. 18, and a summary of the emission components noted in Table 4. The total luminosity from non-thermal processes is ~ 0.5 per cent of the kinetic power in the wind-wind collision ($\sim 10^{36} \text{ erg s}^{-1}$), the latter being ~ 1 per cent of the total kinetic power in the winds. The IC emission dominates for photon energies less than 50 GeV, while the emission from pion decay reaches energies up to 15 TeV (the maximum photon energy from each process is limited by the assumed value of $\gamma_{\text{max}} = 10^5$ for the electrons and ions). The relativistic bremsstrahlung emission is a minor contributor to the total non-thermal flux, and does not dominate at any energy. The absorption of high energy photons by two-photon pair production is significant at GeV and TeV energies, in good agreement with the calculation in Fig. 2 where a single line of sight from the stagnation point of the WCR to an observer was considered.

The IC flux is directly proportional to the energy density of non-thermal electrons, $U_{\text{rel,e}}$, and thus to $\zeta_{\text{rel,e}}$, which in the calculation for Fig. 18 was set to 5.36×10^{-3} as deter-

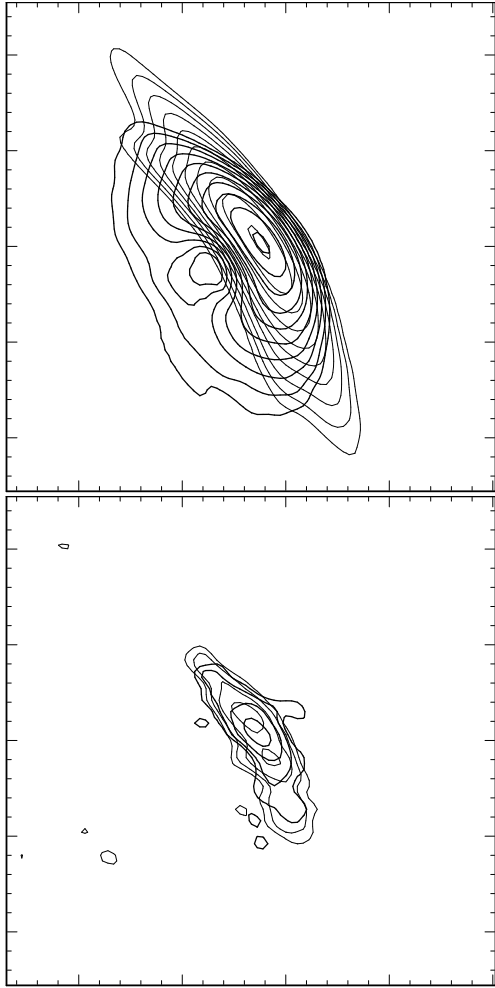


Figure 17. Synthetic VLBA observations generated using the model intensity distributions at 8.4 GHz in Fig. 16, and the same $u-v$ distribution as the observations in Dougherty et al. (2005). The data are scaled to match the peak flux in the observation at phase 0.841 – close to $1.2 \text{ mJy beam}^{-1}$. The top panel shows the intensity for model A (thin) and model B (thick) with no noise. Contours start at $30 \mu\text{Jy beam}^{-1}$ and increase by powers of 1.5. In the lower panel appropriate visibility noise for the VLBA has been included. Contours start at $0.33 \text{ mJy beam}^{-1}$ (which is 3σ in the real data at phase 0.841) and increase by powers of 1.5. Each minor tick mark represents 1 mas, with major ticks at 5 mas intervals. The real data in Dougherty et al. (2005) shows that the WCR is about $10 \times 4 \text{ mas}$ in extent at phase 0.830 and 0.841, which is closely the dimensions of the emission in the lower panel for either model A or B.

mined from the fits of the radio data (Fig. 10). The gradual steepening of the IC spectrum between 2–100 keV (corresponding to $14 \lesssim \gamma \lesssim 100$) indicates the effect of IC cooling on the non-thermal electron energy spectrum. The lack of a clearly defined spectral break reflects the situation for the synchrotron spectrum at radio frequencies (see Figs. 4 and 6 in Pittard et al. 2006). Above 1 MeV, the spectral index is equal to $-p/2 = -0.7$ (corresponding to a photon spectral index, $\Gamma = -\alpha + 1 = (p + 2)/2 = 1.7$).

The relativistic bremsstrahlung spectrum is fairly flat below 1 MeV, and falls off sharply at higher energies. Like

the IC emission, its flux is directly proportional to the specified value of $\zeta_{\text{rel,e}}$. In contrast, the emission from neutral pion decay peaks at $0.5m_\pi c^2 = 67.5 \text{ MeV}$, and, for pions produced from collisions involving non-thermal protons, has a maximum energy of $E_{\text{p,max}}/6$, where the maximum energy of non-thermal protons, $E_{\text{p,max}} = \gamma_{\text{max}} m_p c^2$. The flux from pion-decay is directly proportional to $n_i U_{\text{rel,i}} V$, where n_i is the number density of thermal ions, $U_{\text{rel,i}} = \zeta_{\text{rel,i}} U_{\text{th}}$ is the energy density of non-thermal ions, and V is the volume occupied by the WCR. Since $U_{\text{th}} \propto n_i \propto D^{-2}$, $U_{\text{rel,i}} \propto \zeta_{\text{rel,i}} D^{-2}$. In the adiabatic limit, the volume of the WCR scales as D^3 , so the intrinsic flux from neutral pion decay should scale as $\zeta_{\text{rel,i}} D^{-1}$. As we do not know how (or if) $\zeta_{\text{rel,i}}$ varies with D , the overall dependence on D is unknown. However, since the optical depth from two-photon pair production increases as D^{-1} , the observed flux above 100 GeV may actually decline as D is reduced (the maximum energy of non-thermal ions may also decrease with D – see Sec. 3.3). Table 4 summarizes the emission from the model components in various instrumental bands.

Fig. 18 also compares the non-thermal X-ray and γ -ray emission calculated from our model with the observed ASCA data at $\phi = 0.837$ – dataset 27022010, observed on 1999-10-22. It is reassuring that the model IC fluxes are significantly lower than the observed X-ray emission, consistent with the lack of detection of an underlying power-law component. The O star is in front of the WR star at this orbital phase, and although the IC emission will be slightly higher when a full treatment of the anisotropy of the scattering is accounted for, the increase should be less than a factor of 3 (see Fig. 10 in Reimer, Pohl & Reimer 2005). Such an increase would still leave the IC emission substantially below the thermal X-ray flux. Furthermore, the non-unique radio models have much larger variations in the predicted IC emission (Figs. 19–21). The inset of Fig. 18 shows the intrinsic and attenuated thermal X-ray emission from model B. The attenuated emission is in close agreement with the ASCA data, which adds further support to the value of the O star mass-loss rate in this model.

Models of the radio data alone are ill-constrained (see Sec. 4.3), and the properties of their high energy non-thermal emission provides an important tool for discriminating between the models. In Fig. 19, the high-energy spectra of models A and B, are shown. The flux from model B is slightly higher than from model A because $\zeta_{\text{rel,e}}$ and $\zeta_{\text{rel,i}}$ are slightly higher, and the IC emission has a slightly steeper spectral slope in model B due to stronger IC cooling of the non-thermal electron energy spectrum resulting from the smaller distance between the apex of the WCR and the O star.

Fig. 20 shows the high energy non-thermal emission from models C, D, and E. The degeneracy of the emission at radio wavelengths is broken at high energies where clear differences in the models occur. In particular, the decrease in p from model C ($p = 1.53$) to model E ($p = 1.1$) is clearly manifest in the spectral slope, while the increase in $\zeta_{\text{rel,e}}$ from model C to E is apparent in the relative normalization of the spectra. Since model E has $\zeta_{\text{rel,e}} = 2.8 \times 10^{-2}$ which precludes setting $\zeta_{\text{rel,i}} = 100 \zeta_{\text{rel,e}}$, we instead set $\zeta_{\text{rel,i}} = 30 \zeta_{\text{rel,e}}$ for this model.

The high energy non-thermal emission from models B and F are compared in Fig. 22. The spectral slope of the

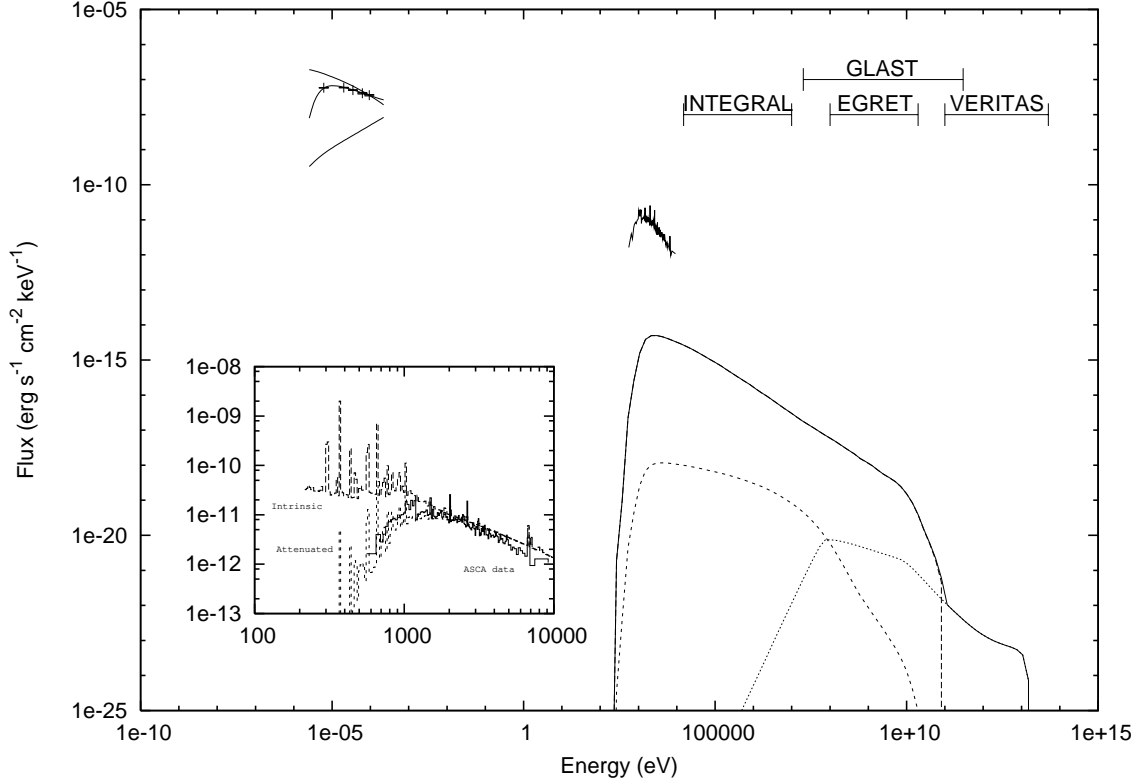


Figure 18. The radio, and non-thermal UV, X-ray and γ -ray emission calculated from model B, together with the observed radio and X-ray flux. The radio model shown indicates the thermal free-free flux (displayed below the data points), the *intrinsic* synchrotron flux before free-free absorption (displayed above the data points), and the total observed emission (cf. Fig. 10). The model IC (long dash), relativistic bremsstrahlung (short dash), and pion decay (dotted) emission components are shown, along with the total emission (solid). Photoelectric absorption is significant at soft X-ray energies up to ~ 2 keV. To calculate the IC and relativistic bremsstrahlung emission, $\zeta_{\text{rel,e}} = 5.36 \times 10^{-3}$, as derived from the fit to the radio data (Fig. 10) was assumed. $\zeta_{\text{rel,i}} = 100 \zeta_{\text{rel,e}}$ was assumed to calculate the neutral pion decay emission. The observed *ASCA* X-ray spectrum from $\phi = 0.837$ is also shown. The intrinsic (dashed line) and attenuated (dotted line) thermal X-ray emission from model B is displayed in the inset, where we have assumed unmodified collisional shocks, rapid thermalization of the post-shock electrons, and collisional ionization equilibrium in our model. The ISM absorbing column was fixed at $N_{\text{H}} = 5.4 \times 10^{21} \text{ cm}^{-2}$ (Zhekov & Skinner 2000), and the absorption coefficients for the ISM and the WR and O star winds were calculated using Cloudy v94.00 (Van Hoof, Martin & Ferland 2000, see <http://www.nublado.org>).

Table 4. The high energy non-thermal emission from model B of WR 140 at orbital phase 0.837, with $\eta = 0.02$ and $\zeta_{\text{rel,e}} = 5.36 \times 10^{-3}$. $\zeta_{\text{rel,i}} = 100 \zeta_{\text{rel,e}}$ is assumed for the calculation of the emission from neutral pion decay. The IC emission dominates the total emission in each energy band noted in this table.

Mechanism	Total emission (erg s^{-1})	EGRET (100MeV-20GeV) (erg s^{-1})	EGRET (100MeV-20GeV) ($\text{photons s}^{-1} \text{ cm}^{-2}$)	INTEGRAL IBIS (15keV-10MeV) ($\text{photons s}^{-1} \text{ cm}^{-2}$)	GLAST (20MeV-300GeV) ($\text{photons s}^{-1} \text{ cm}^{-2}$)
Inverse Compton	3.5×10^{33}	2.5×10^{33}	5.5×10^{-9}	2.7×10^{-6}	1.5×10^{-8}
Rel. bremsstrahlung	1.8×10^{30}	3.2×10^{29}	2.5×10^{-12}	2.0×10^{-9}	2.1×10^{-11}
π^0 decay	6.8×10^{31}	1.4×10^{31}	1.4×10^{-11}	3.9×10^{-14}	1.8×10^{-11}

IC emission at energies greater than 0.1 MeV reflects the different values of p in these models. This emission arises predominantly from those electrons near the apex of the WCR with initial post-shock Lorentz factors greater than ~ 100 . All such electrons rapidly cool to Lorentz factors of approximately 12 (model B) and 25 (model F) before advecting out of the system. Although the absorption of γ -rays by pair-production is lessened in model F due to the reduced stellar luminosities assumed, the commensurate reduction in

$\zeta_{\text{rel,e}}$ (and thus $\zeta_{\text{rel,i}}$) and the increase in p lead to an overall decrease in the VERITAS flux (Table 5).

Fig. 21 shows a comparison between the high energy non-thermal emission from models where free-free absorption (model B) or the Razin effect (models G, H, I and J) is responsible for the low frequency radio turnover. The predicted non-thermal emission from model G exceeds the observed *thermal* emission at X-ray energies, and so this model can be immediately excluded. For models H-J the

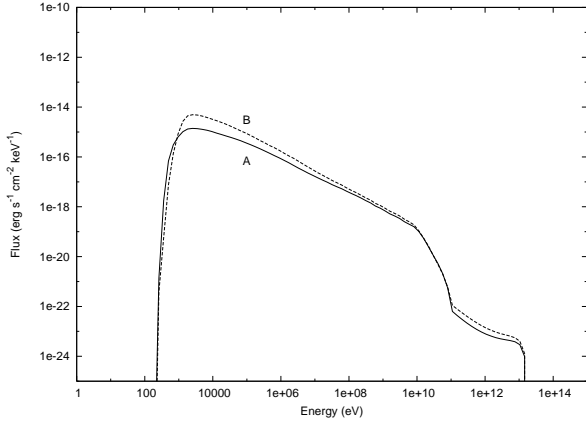


Figure 19. The high energy non-thermal emission calculated from models A and B with $p = 1.4$.

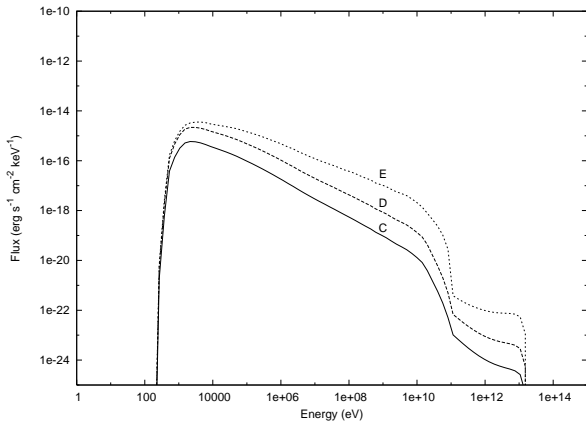


Figure 20. The high energy non-thermal emission calculated from models C, D and E, with $\eta = 0.11$.

non-thermal emission is significantly lower than the thermal X-ray flux, so they cannot be excluded in the same manner, though there are other reasons why they are less desirable than model B (see Sec. 4.3.2). The large values of $\zeta_{\text{rel,e}}$ in models H-J cause the IC flux to be ~ 2 orders of magnitude higher relative to model B, and future observations with INTEGRAL, AGILE, and GLAST could discriminate between these models. Table 5 notes the non-thermal luminosities and fluxes in various energy bands from each model.

4.4.2 Comparison to observations

The total photon flux in the EGRET band from models A-F (where free-free absorption is responsible for the low frequency radio turnover) varies from $4.9 \times 10^{-10} \text{ photonss}^{-1} \text{ cm}^{-2}$ (model C) to $4.2 \times 10^{-8} \text{ photonss}^{-1} \text{ cm}^{-2}$ (model E). The highest prediction is still below the flux detected from 3EG J2022+4317 during the December 1992 observation at $\phi = 0.97$. While the different orbital phases of the radio and EGRET data prevent a direct comparison, the IC emission should increase between phase 0.837 and 0.97 as the stellar separation decreases by about a factor of three, so the models with the highest pre-

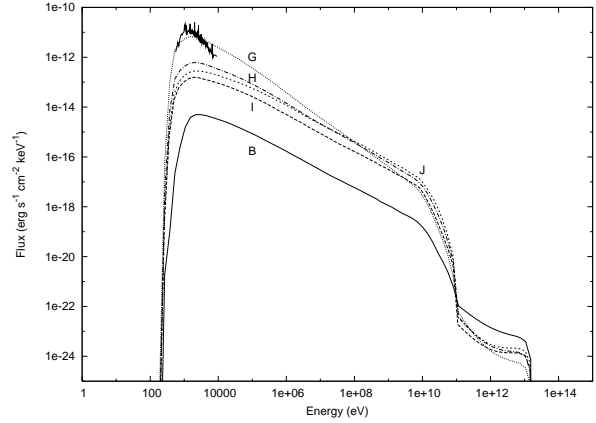


Figure 21. The high energy non-thermal emission calculated from models B, and G–J. The low frequency radio turnover in model B is due to free-free absorption, while in models G–J it is due to the Razin effect. The ASCA data are also shown.

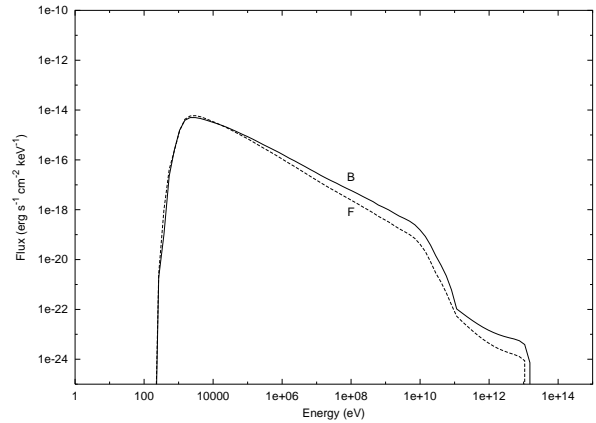


Figure 22. The high energy non-thermal emission calculated from models B and F, with $\eta = 0.02$.

dicted fluxes are at least consistent with the data. Models G, H and J have predicted photon fluxes in the EGRET band which exceed that observed from 3EG J2022+4317, which is an additional reason why these fits are not as desirable as those where free-free absorption is responsible for the low frequency radio turnover.

In model B, the photon spectral index of the total non-thermal emission, Γ , is -2.9 at 1 keV (due to photoelectric absorption), 1.7 at 1 MeV and 100 MeV , 1.8 at 1 GeV , and 3.5 at 20 GeV , and is in rough agreement with the observed EGRET value of $\Gamma = 2.31 \pm 0.19$ between $100 \text{ MeV} - 20 \text{ GeV}$. Model E has the flattest non-thermal spectrum, with $\Gamma = -1.0$ at 1 keV , 1.55 at 1 MeV and 100 MeV , 1.6 at 1 GeV , and 2.6 at 20 GeV , and matches the observed spectral slope less well.

4.4.3 Comparison to previous work

The non-thermal γ -ray emission from WR 140 has previously been estimated by Benaglia & Romero (2003) and Reimer, Pohl & Reimer (2005). Since Benaglia & Romero's calculations are based on a stellar separation of 10 AU (cor-

Table 5. The high energy non-thermal emission calculated from the models in Table 3.

Model	Total emission (erg s^{-1})	EGRET (100MeV-20GeV) (erg s^{-1})	EGRET (100MeV-20GeV) (photons $\text{s}^{-1} \text{cm}^{-2}$)	INTEGRAL IBIS (15keV-10MeV) (photons $\text{s}^{-1} \text{cm}^{-2}$)	GLAST (20MeV-300GeV) (photons $\text{s}^{-1} \text{cm}^{-2}$)	VERITAS (100GeV-50TeV) (photons $\text{s}^{-1} \text{cm}^{-2}$)
A	2.4×10^{33}	1.8×10^{33}	3.4×10^{-9}	1.0×10^{-6}	1.0×10^{-8}	4.9×10^{-14}
B	3.6×10^{33}	2.5×10^{33}	5.5×10^{-9}	2.7×10^{-6}	1.5×10^{-8}	8.4×10^{-14}
C	3.2×10^{32}	2.1×10^{32}	4.9×10^{-10}	3.0×10^{-7}	1.4×10^{-9}	7.3×10^{-15}
D	2.8×10^{33}	2.0×10^{33}	4.1×10^{-9}	1.5×10^{-6}	1.1×10^{-8}	5.3×10^{-14}
E	3.6×10^{34}	2.6×10^{34}	4.2×10^{-8}	4.2×10^{-6}	9.4×10^{-8}	4.3×10^{-13}
F	1.3×10^{33}	8.0×10^{32}	2.0×10^{-9}	2.4×10^{-6}	6.3×10^{-9}	3.5×10^{-14}
G	2.4×10^{35}	8.3×10^{34}	2.8×10^{-7}	1.4×10^{-3}	1.1×10^{-6}	2.7×10^{-14}
H	1.9×10^{35}	1.3×10^{35}	3.1×10^{-7}	2.7×10^{-4}	9.5×10^{-7}	2.3×10^{-14}
I	1.1×10^{35}	7.8×10^{34}	1.7×10^{-7}	8.1×10^{-5}	4.7×10^{-7}	1.3×10^{-14}
J	2.4×10^{35}	1.8×10^{35}	4.0×10^{-7}	1.7×10^{-4}	1.1×10^{-6}	2.3×10^{-14}

responding to $\phi = 0.95$), neither our estimates, their estimates, or the EGRET detections, can be directly compared. Their estimate for the IC luminosity in the EGRET band of $2.1 \times 10^{34} \text{ erg s}^{-1}$ is typically higher than the values from our models A–F, but lower than those from models G–J (cf. Table 5).

There are substantial differences between this work and that of Benaglia & Romero (2003): their estimate is obtained through the use of Eq. 2, in which the ratio of the IC to synchrotron emission depends strongly on the B-field, and is based on only a single position in the WCR. They estimate that $B = 200 \text{ mG}$ (although noting its value is quite uncertain). In contrast, here the IC emission is determined from models of the radio emission. The magnetic field is a fitted (though ill-constrained) parameter of the models, with a maximum at the stagnation point², and rapidly declines in the downstream flow. Also, in the approach presented here the B-field directly affects the synchrotron emission, but also indirectly affects the calculations of the high energy emission which depend on the population and spatial distribution of non-thermal particles i.e. $\zeta_{\text{rel,e}}$ and $\zeta_{\text{rel,i}}$. Finally, Benaglia & Romero (2003) use the *observed* synchrotron luminosity, rather than the intrinsic luminosity, leading to an underestimate of the IC luminosity.

Our estimates for the relativistic bremsstrahlung luminosity are broadly consistent with the limit of $< 10^{32} \text{ erg s}^{-1}$ noted in Benaglia & Romero (2003), but the pion decay luminosities are wildly discrepant with our lowest estimate being 10 orders of magnitude lower. Details of their calculation are noted in Benaglia et al. (2001), where a “cosmic ray enhancement factor” of 10 is assumed. This factor is the ratio between the cosmic ray energy density at the source (in this case the WCR) and that observed at the Earth (which is roughly equal to the average cosmic ray energy density within the Galaxy of $\approx 1 \text{ eV cm}^{-3} = 1.6 \times 10^{-12} \text{ erg cm}^{-3}$). However, at the head of the WCR, the energy density of relativistic ions in our model B, for example, is $\approx 0.64 \text{ erg cm}^{-3}$. This corresponds to a cosmic ray enhancement factor of

$\sim 10^{11}$, and accounts for the large underestimate of the pion decay emission by Benaglia & Romero (2003).

Reimer, Pohl & Reimer (2005) have also calculated the expected high energy non-thermal flux from WR 140. They conclude that the change in the IC flux with viewing angle due to anisotropic scattering is likely to be obscured by large variations in the energy density of the stellar radiation fields resulting from the high orbital eccentricity. While anisotropic IC emission and Klein-Nishina effects are clearly processes which should be included in future models, other uncertainties, such as the value of p , currently have a greater influence on the IC emission.

4.4.4 Predictions for forthcoming instruments

Our predictions for the flux in the energy band of the IBIS instrument onboard INTEGRAL and the GLAST large area telescope (LAT) are also noted in Table 5. For models A–F the predicted fluxes are $\sim 10^3 \times$ lower in the INTEGRAL band, and $\sim 10^2 \times$ lower in the GLAST band than those made by Benaglia & Romero (2003). Using the INTEGRAL Observing Time Estimator³, we find that model A cannot be detected at the 5σ level in the 15 keV – 10 MeV range using the IBIS imager, since an exposure time of 300 yrs is required! Model E, the brightest of models A–F in this band, still requires an exposure of 180 yrs. With several bright sources (including Cyg X-1) nearby, the required exposure time may be even longer. On the other hand, for model J an exposure time of only 2.8 Msec is needed. At the time of writing, WR 140 is not detected in a 2 Msec exposure (De Becker 2005), and we are close to ruling out model J (and H) on this basis. Line emission at γ -ray energies from the de-excitation of nuclear isomers, such as $^{12}\text{C}^*$ and $^{16}\text{O}^*$, is much too faint to be detected with current instrumentation (Benaglia & Romero 2003).

The GLAST 5σ sensitivity at $E > 100 \text{ MeV}$ for sources at high galactic latitudes with a $\Gamma = 2$ spectrum after a 2 yr all-sky survey is $1.6 \times 10^{-9} \text{ photons s}^{-1} \text{cm}^{-2}$. Therefore, our predictions suggest that WR 140 will be detectable, this being important to differentiate between the models in Table 5.

² Since the magnetic field is not well constrained by the radio fits, there is a large variation in its strength between models. For instance, at the apex of the WCR, $B = 74 \text{ mG}$ in model G, rising to 3.3 G in model C, and is 1.2 G in our preferred model (B).

³ <http://integral.esac.esa.int/isoc/operations/html/OTE.html>

At energies of approximately 50 GeV and higher, the flux from the models arises exclusively from the decay of neutral pions. The high energy cut off is ≈ 15 TeV. The VERITAS array is sensitive to γ -rays in the 50 GeV to 50 TeV energy band, but unfortunately the high absorption from two-photon pair production severely reduces the photon flux above ~ 10 GeV. The predicted flux from model B is not sufficient for a detection in a 50 hr observation, and we conclude that WR 140 is probably too faint to be detected at $\phi = 0.837$, though it might be brighter at phases closer to periastron. An observation by GLAST, for example, will better constrain the potential models, and allow more robust predictions of the flux at \sim TeV energies.

5 DISCUSSION

5.1 Mass-loss rates of early-type stars

It is important that accurate measurements of mass-loss rates from early-type stars are obtained, as mass-loss is known to significantly affect their evolution, and the injection of mass, momentum and energy influences not only the gas-phase conditions in the immediate environment of the clusters within which the massive stars form, but also the phase structure and energetics of the ISM on galactic scales, and the thermodynamics and enrichment of the intergalactic medium on Mpc scales and above.

Unfortunately, observational determinations of mass-loss rates are often highly uncertain, in part because many of the techniques are sensitive to the degree of structure in the winds. Overestimates by factors of at least 3 or more are likely when the winds are clumpy, but for some types of O stars it could be as high as factors of 20 or more (Fullerton, Massa & Prinja 2005). The X-ray emission from CWB systems provides an opportunity to measure mass-loss rates using a method which is not expected to be very sensitive to clumping (see Sec. 4.2.3). In fact, mass-loss rates could be underestimated using this technique: at least some winds may be both denser and faster at high latitudes (Dwarkadas & Owocki 2002; Smith 2002; Chesneau et al. 2005), and if the stellar rotation axes of the stars are closely perpendicular to the orbital plane, the WCR then probes those parts of the winds which are less dense and slower. In addition, a significant amount of energy may be siphoned into particle acceleration. In this work, the mass-loss rate for the O supergiant star in WR 140 is towards the lower end of previous estimates, but is consistent with expected biases. A reduction in mass-loss rates, and/or mass-loss through a predominantly polar flow, can also explain the near-symmetry of observed X-ray lines from early-type stars (Owocki & Cohen 2006; Mullan & Waldron 2006; Cohen et al. 2006), and both reduced mass-loss and polar flow help in the theoretical formation of gamma-ray bursts (Woosley & Heger 2006).

5.2 The nature of shocks and particle acceleration in wide CWB systems

In this work we have presented evidence for a fairly flat spectrum of non-thermal electrons in WR 140, which is further supported by earlier fits to the radio data of WR 147 (this

was mistakenly interpreted as evidence for shock modification in Pittard et al. 2006). A spectral index of $p < 2$ suggests multiple shock acceleration, where particles injected and accelerated at a shock are advected through many additional shocks further downstream. At each shock the non-thermal particles are re-accelerated, and the spectral index in the limit of many shocks approaches $p = 1$. If the electrons suffer energy losses between the accelerating shocks, p can become even smaller (Schlickeiser 1984; Melrose & Crouch 1997).

In CWB systems, the stellar winds are thought to contain wind-embedded shocks due to the line de-shadowing instability of the radiative driving (e.g., Owocki, Castor & Rybicki 1988). This appears to provide the ideal opportunity for re-acceleration and hardening of the non-thermal particle spectrum prior to the global shocks bounding the WCR, where a large amount of wind power is put into these seed particles (along with newly accelerated particles) to create a spectrum with $p < 2$. However, we caution that re-acceleration has not yet been demonstrated in theoretical calculations of wind-embedded shocks, because in one-dimensional simulations the structure of each wind-embedded shock is such that the accelerated particles are trapped between forward and reverse shocks. This has posed a problem for the interpretation of non-thermal radio emission from single stars (Van Loo, Runacres & Blomme 2006), and only calculations which use a phenomenological shock model are currently successful in fitting the data (e.g., Chen & White 1994). The expectation is that higher dimension models of instability-generated structure (see, e.g., Dessart & Owocki 2003) will allow accelerated particles to escape one shock and be re-accelerated at others.

We can speculate about additional effects which occur in CWB systems with highly eccentric orbits. For example, the number of wind-embedded shocks that accelerate a non-thermal particle prior to the WCR may change significantly with orbital phase, leading to a phase dependent p . Similarly, if the obliquity of the shocks changes with stellar separation, the injection efficiency and rate of particle acceleration may also alter. In addition, it is likely that the maximum energy obtained by electrons and ions varies with stellar separation, and any or all of these effects may change the degree of shock modification around the orbit. Finally, the assumption of isotropic synchrotron emission will need to be reconsidered if the magnetic turbulence is low enough that the mean B-field has a preferred direction.

In the context of WR 140, these are all potential explanations for the observed asymmetry of the radio lightcurve. The siphoning of pre-shock energy into particle acceleration may also explain the behaviour of the X-ray lightcurve, which does not follow the expected $1/D$ variation for an adiabatic WCR (Pollock, Corcoran & Stevens 2002). In the present work, the temperature of the thermal X-ray emission from calculations of unmodified collisional shocks is higher than observed. This may be a sign of shock modification, in addition to the more common suggestion that $T_e < T_i$ immediately postshock.

Finally, CWB systems have B-fields which are sufficiently high to cause significant energy to be transferred from the non-thermal particles into magnetic turbulence via Alfvén wave heating, thereby lowering the acceleration efficiency. Therefore, it is unlikely that compression ratios as

extreme as those possible at the reverse shock of SNRs (Ellison, Decourchelle & Ballet 2005) will occur in CWB systems.

5.3 Non-thermal X-ray, TeV and neutrino emission from CWBs

While there is no observational evidence for non-thermal X-ray emission in WR140, there are some systems that appear to show a power-law tail. Perhaps the strongest candidate is η Carinae, where X-rays at energies of up to 150 keV were detected during a long BeppoSAX exposure (Viotti et al. 2004). Determining the spectral slope at higher energies should allow discrimination of the competing models proposed to explain this emission.

The lack of observed non-thermal X-ray emission from CWB systems which are known non-thermal radio emitters (De Becker et al. 2004a, 2005, 2006) contrasts with the possible detection of non-thermal X-ray emission from HD 159176, which is not known to be a non-thermal radio emitter (De Becker et al. 2004b). However, the IC losses in HD 159176 with its 3.4 d orbital period will be catastrophic, and it is therefore not surprising that non-thermal X-ray emission is possibly seen while there is no clear signature of synchrotron emission (De Becker 2005).

In the models of WR140 presented in this paper, absorption of high energy photons by pair-production creates a very steep photon spectrum between 10 GeV and 1 TeV. Consequently, the photon flux above 1 TeV is about an order of magnitude lower than the flux predicted in the VERITAS bandpass, which is dominated by photons with energies less than 1 TeV (see Table 5). For example, in model B the flux above 1 TeV is 1.2×10^{-14} photons $\text{s}^{-1} \text{cm}^{-2}$. Despite the possibility of high absorption, the flux from CWB systems compares favourably to some other mechanisms proposed for the generation of TeV emission, such as the interaction of cosmic rays in the innermost parts of the winds of early-type stars (Torres, Domingo-Santamaría & Romero 2004) or within the cluster wind of a dense stellar cluster (Domingo-Santamaría & Torres 2006). Therefore, it is possible that several CWBs or multiple colliding winds from a cluster of stars contribute part or all of the flux from the unidentified TeV source detected in the Cygnus region, TeV J2032+4130 (Aharonian et al. 2005a), which has an integral flux $F_\gamma(E_\gamma > 1 \text{ TeV}) = 6.9(\pm 1.8) \times 10^{-13}$ photons $\text{s}^{-1} \text{cm}^{-2}$. Another possible scenario noted by Aharonian et al. (2005a) involves particle acceleration at a termination shock where a relativistic jet from Cygnus X-3 encounters the ISM. The unidentified TeV source HESS J1813-178 (with an integrated flux above 200 GeV of 1.2×10^{-12} photons $\text{s}^{-1} \text{cm}^{-2}$) may also be associated with an OB association (Aharonian et al. 2005b).

The $\nu_\mu + \bar{\nu}_\mu$ neutrino flux from the decay of charged pions can be estimated from the γ -ray flux produced by neutral pion-decay by imposing energy conservation (Alvarez-Muñiz & Halzen 2002). For model B, the predicted signal in a 1 yr observation with ICECUBE is 0.15 interactions, rising to about 1–2 interactions for model E. Therefore, we do not expect CWB systems to be strong sources for detection with neutrino telescopes. This is contrary to the conclusion of Bednarek (2005), who adopted a much higher efficiency for conversion of the kinetic power of the

stellar winds into non-thermal particles, due largely to the assumption of $\eta = 1$.

5.4 Colliding winds in dense stellar clusters

Our work is also relevant to more complicated systems involving colliding winds, such as dense stellar clusters. Hydrodynamical simulations of the multiple colliding winds in clusters have been performed by Raga et al. (2001), with particular application to the Galactic Centre in Coker & Melia (1997), Coker & Pittard (2005), Rockefeller et al. (2005), and Cuadra et al. (2006). A network of bubbles forms around the stars, which are embedded in a medium of hot shocked gas. Highly non-linear DSA should occur at the stellar termination shocks in stellar clusters if the pre-shock B-field is small enough ($B \lesssim 10 \mu\text{G}$, Ellison, Decourchelle & Ballet 2005), though the most extreme modification (e.g., compression ratios much greater than 4) will occur only at the cluster's edge.

Shock modification is also a potential explanation for the lower than expected temperature of the X-ray emitting gas observed in several dense stellar clusters (e.g., Stevens & Hartwell 2003), though mass-loading and slow equilibration of the post-shock ion and electron temperatures are other possibilities. In addition, the X-ray luminosities of the diffuse gas are generally higher than expected, which indicates mass-loading and/or a low thermalization efficiency (Stevens & Hartwell 2003; Oskinova 2005), the latter also being consistent with efficient particle acceleration and shock modification. If the rate at which energy is removed from the cluster (for example, by radiative cooling) exceeds 30 per cent of the energy injection rate, a time independent cluster wind cannot form (Silich, Tenorio-Tagle & Rodríguez-González 2004). Though the removal of energy through particle acceleration was not considered, efficiencies of this order are expected (e.g., Bykov 1999), in which case a full time-dependent solution for the cluster wind is required.

Amongst the dense stellar clusters known in our Galaxy, the central cluster around Sgr A* is unusual in many respects, including the recent detection of apparently thermal gas with a temperature $kT \approx 8 \text{ keV}$ (Muno et al. 2004), and TeV emission. Observations with HESS show a 1–10 TeV luminosity of $\sim 10^{35} \text{ erg s}^{-1}$ (Aharonian et al. 2004). The upper limit on the TeV source size is $< 3'$ (95 per cent confidence level), which corresponds to $< 7 \text{ pc}$ at the distance of the Galactic Centre. The photon spectrum above the 165 GeV threshold is specified by $F(E) = F_0 E_{\text{TeV}}^{-\Gamma}$, with $\Gamma \approx 2.2$ and $F_0 \approx 2.5 \times 10^{-12}$ photons $\text{s}^{-1} \text{cm}^{-2} \text{TeV}^{-1}$, and has been independently confirmed with MAGIC (Albert et al. 2006). Various origins of the TeV emission have been proposed, including the central supermassive black hole (Aharonian & Neronov 2005a), the young supernova remnant Sgr A East (Crocker et al. 2005), the dark matter halo (Horns 2005), and from non-thermal particles accelerated at the multiple colliding winds shocks (Quataert & Loeb 2005), which we now discuss.

The total wind power estimated from the cluster of stars within $\sim 10''$ ($\sim 0.4 \text{ pc}$) of the Galactic Centre is $\sim 3 \times 10^{38} \text{ erg s}^{-1}$. In the context of colliding winds, the TeV emission may arise from IC upscattering of ambient photons by non-thermal electrons, or from the decay of neu-

tral pions created by the collisions of non-thermal and thermal hadrons. It is likely that IC cooling limits the maximum Lorentz factor that non-thermal electrons within the central parsec can attain to $\sim 10^7$ (Quataert & Loeb 2005), which is only marginally high enough for IC scattering to account for the detected TeV flux. The TeV emission occurs from electrons whose cooling time is less than the flow time out of the cluster i.e. from those with $\gamma > \gamma_c$. For a power-law distribution of electrons $n(\gamma) \propto \gamma^{-p}$, the IC photon spectral index is $\Gamma = (p + 2)/2$, for $\gamma > \gamma_c$. Hence the TeV spectral index of 2.2 implies that $p \approx 2.4$, which is much softer than we find here from CWBs, and also for the theoretical limit for multiple shocks ($p=1.0$, Pope & Melrose 1994). This implies that re-acceleration at multiple shocks within the cluster, as proposed by Ozerov, Genzel & Usov (1997), does not occur.

It is possible to imagine several reasons why this might be the case. Firstly, there is unlikely to be a seed population of non-thermal particles from wind-embedded shocks encountering the termination shock of the winds because of the large adiabatic cooling experienced as the plasma flows out to $\sim 0.01 - 0.1$ pc. Hence, the particle spectrum at the termination shocks is likely to have $p = 2$. Secondly, it is not entirely clear that there will be numerous opportunities for particle re-acceleration within the radius of the cluster, since the cooling timescale of the shocked gas is long, and it remains hot. Analytical solutions of cluster winds reveal that the shocked gas, on average, only becomes supersonic at the outer radius of the cluster (Chevalier & Clegg 1985). Within the cluster interior, the network of hot post-shock gas is mostly subsonic, and while it experiences pressure gradients and weak shocks as it escapes, in general it is not likely to be repeatedly shocked. This lack of opportunity for re-acceleration means that p is likely to remain close to the value obtained from a single shock.

Alternatively, the detected TeV emission from the Galactic Centre may arise from the decay of neutral pions. In the context of multiple colliding winds, Ozerov, Genzel & Usov (1997) estimate the emission from pion-decay to be $\sim 3 \times 10^{36} \text{ erg s}^{-1}$, assuming 10 per cent acceleration efficiency for hadrons at the multiple shocks, and a 10 per cent energy transfer into pions i.e. a 1 per cent efficiency overall. Other estimates in the literature suggest a somewhat lower luminosity from this process (e.g., Quataert & Loeb 2005). If neutral pions are responsible, the observed spectral index may indicate that $p \approx 2.2$. The inferred value of p from both the IC and pion-decay mechanisms implies particle acceleration at low Mach number shocks ($M \approx 3$ and $M \approx 5$, respectively) within the network of hot shocked gas. This conclusion does not rule out the possibility of modification at the termination shocks of the individual winds, which would be consistent with the low X-ray temperature of the cooler emission component ($kT \approx 0.8$ keV, Munro et al. 2004).

The Galactic Centre region has also been detected at GeV energies. The observed luminosity of the EGRET source 3EG J1745-2852 is $\approx 2 \times 10^{37} \text{ erg s}^{-1}$ (Mayer-Hasselwander et al. 1998; Hartman et al. 1999). However, while its position is consistent with Sgr A*, the angular resolution of 1° covers a solid angle about 100 times larger than the emission seen with HESS. As the EGRET spectrum is about 4 orders of magnitude brighter than the

observed HESS emission extrapolated as a power-law to GeV energies, different processes/sources may well be responsible for the detected emission (although different assumptions concerning the injection spectrum and diffusion coefficients of non-thermal protons may account for both observations, as shown by Aharonian & Neronov 2005b). Regardless of the origin of non-thermal protons, if the emission is from pion-decay, a substantial TeV neutrino flux should be seen by neutrino telescopes.

While it remains difficult to draw firm conclusions on the nature of the TeV emission observed from the Galactic Centre, we note that the nearby Arches cluster, which has an integrated mass-loss rate from its stellar components within an order of magnitude of the Galactic Centre cluster, has not yet been detected at TeV energies. This may argue against the cluster wind scenario as an explanation for the TeV emission.

6 SUMMARY AND FUTURE DIRECTIONS

In this paper we have applied models to the observed emission from WR 140 at $\phi = 0.837$, when the radio emission is near maximum, and when X-ray data are available. Simultaneous fits to the radio and X-ray data lead to a determination for the wind momentum ratio of $\eta = 0.02$, with mass-loss rates $\dot{M}_{\text{WR}} \approx 4.3 \times 10^{-5} \text{ M}_\odot \text{ yr}^{-1}$ and $\dot{M}_\text{O} \approx 8 \times 10^{-7} \text{ M}_\odot \text{ yr}^{-1}$. While the O star mass-loss rate is substantially lower than the values estimated by Repolust et al. (2004) for O4–5 supergiants, an order of magnitude reduction in the mass-loss rate is consistent with the recent estimates of Fullerton, Massa & Prinja (2005), and with some current explanations of the observed near-symmetry of X-ray lines. Such sizeable reductions have extensive implications for massive star evolution (including gamma-ray bursts), and feedback on the interstellar medium. There is also some scope for reducing the stellar luminosities adopted from Dougherty et al. (2005).

A key finding is that models of the radio data require $p < 2$. This suggests the occurrence of particle re-acceleration at multiple wind-embedded shocks prior to the WCR. A flatter spectrum for the non-thermal particles has important implications for the modelling of the high energy non-thermal emission from such systems, with almost all previous models in the literature assuming that $p = 2$. While our fits are currently non-unique, models where the Razin effect is responsible for the low frequency radio turnover (which allow $p = 2$) can be ruled out on the basis that the implied efficiency of electron acceleration is extraordinarily high. Further, they predict the detection of IC emission by INTEGRAL which has not yet been achieved, and in some cases non-thermal X-ray emission at fluxes higher than the observed thermal emission. Observations with Suzaku should be more sensitive than those made with INTEGRAL, and may allow the detection of non-thermal X-ray emission.

We also clearly demonstrate that the observed thermal X-ray emission is softer than obtained from theoretical models which assume unmodified shocks with rapid thermalization of the post-shock electrons. In previous work this has been interpreted as evidence for weak electron heating behind the shocks (Zhekov & Skinner 2000; Pollock et al. 2005), but shock modification may also have a role to

play (this is not necessarily mutually exclusive with our requirement for particle re-acceleration). Modified shocks have weaker subshocks, which reduces the temperatures in the post-shock plasma. Modification is expected if the efficiency of particle acceleration is high enough that a significant fraction (of order 50 per cent) of the pre-shock energy is put into non-thermal particles. Indeed, our preferred model (B) places a comparable amount of energy into accelerated particles if we assume that there is 100 times more energy put into ions than into electrons. Even higher efficiencies are expected if the postshock B-field is lower than in model B which is approximately 1 G at the apex of the WCR. Since the high B-fields in CWBs are likely to prevent highly non-linear compression ratios, any modification may instead be dominated by particle loss due to the curvature of the shocks. Larger non-linear effects, comparable to those possible at the reverse shock in SNRs (Ellison, Decourchelle & Ballet 2005), may occur at the wind-wind collisions in stellar clusters where the B-field is much lower.

The high energy non-thermal emission from WR 140 is expected to display significant variability with orbital phase, as p and the degree of shock modification change. We emphasize that the future detection of TeV emission from CWB systems will almost certainly indicate pion-decay, since the high photon fluxes prevent the acceleration of electrons beyond $\gamma \sim 10^5 - 10^6$. WR 140, along with WR 146 which has the brightest non-thermal radio emission of any CWB (Dougherty, Williams & Pollacco 2000), and WR 147 which is the widest CWB system on the sky (Williams et al. 1997) and the only system resolved in X-rays (Pittard et al. 2002), present an ideal opportunity for the unambiguous detection of pion-decay from accelerated ions. The estimated flux of TeV photons from CWB systems compares favourably to some other mechanisms, and may contribute part or all of the flux from some TeV sources. The multiple colliding winds in the Galactic Center cluster may make a non-negligible contribution to the observed TeV flux. However, CWB systems are not expected to be strong neutrino sources.

Tighter constraints on p and the nature of the shocks and particle acceleration in colliding winds systems (binaries and clusters) are best achieved through the dual strategy of improving the theoretical models and obtaining observational data at MeV and GeV energies. On the theoretical side models should explicitly account for the transfer of part of the available pre-shock energy into accelerated particles, self-consistently account for the maximum energy obtained by the non-thermal electrons and ions, and include Klein-Nishina effects and anisotropic IC scattering. Upcoming observations by AGILE and GLAST at MeV and GeV energies where the emission is no longer degenerate with B and p should then distinguish between the non-unique model fits to the radio data, and determine the B-field in the WCR and the spectral index of the non-thermal particles.

ACKNOWLEDGMENTS

We have had many interesting discussions during the course of this work, and would like to thank Felix Aharonian, Paula Benaglia, Andrei Bykov, Paul Crowther, Chuck Dermer, Jamie Holder, Jim MacDonald, Anita Reimer, Sven

van Loo, and Perry Williams. We would also like to thank Mike Corcoran for supplying the ASCA X-ray spectrum of WR 140, Rob Coker for comments on an earlier draft, and Evan O'Connor for running some early models. Johannes Knapp, Andy Pollock, Ian Stevens, and Perry Williams provided helpful comments prior to submission. Special thanks go to Don Ellison for his tireless response to questions over the course of the last few years. SMD gratefully acknowledges partial funding for a visit to Leeds. JMP is supported by a University Research Fellowship from the Royal Society. This research has made use of NASA's Astrophysics Data System Abstract Service.

REFERENCES

- Aharonian F. A., Atoyan A. M., 1996, *A&A*, 309, 917
- Aharonian F. A., et al. (HESS collaboration), 2004, *A&A*, 425, L13
- Aharonian F. A., et al. (HEGRA collaboration), 2005a, *A&A*, 431, 197
- Aharonian F. A., et al. (HESS collaboration), 2005b, *Science*, 307, 1938
- Aharonian F. A., Neronov A., 2005a, *ApJ*, 619, 306
- Aharonian F. A., Neronov A., 2005b, *Astr. Space Sci.*, 300, 255
- Albert J., et al. (MAGIC collaboration), 2006, *ApJ*, 638, L101
- Alvarez-Muñiz J., Halzen F., 2002, *ApJ*, 576, L33
- Bamba A., Yamazaki R., Ueno M., Koyama K., 2003, *ApJ*, 589, 827
- Baring M. G., Harding A. K., 1997, *ApJ*, 491, 663
- Baring M. G., Ellison D. C., Reynolds S. P., Grenier I. A., Goret P., 1999, *ApJ*, 513, 311
- Bednarek W., 2005, *MNRAS*, 363, L46
- Bell A. R., 2004, *MNRAS*, 353, 550
- Benaglia P., Romero G. E., Stevens I. R., Torres D. F., 2001, *A&A*, 366, 605
- Benaglia P., Romero G. E., 2003, *A&A*, 399, 1121
- Berezhko E. G., Ellison D. C., 1999, *ApJ*, 526, 385
- Berezhko E. G., Elshin V. K., Ksenofontov L. T., 1996, *JETP*, 82, 1
- Berezhko E. G., Ksenofontov L. T., Völk H. J., 2003, *A&A*, 412, L11
- Berezhko E. G., Völk H. J., 2004, *A&A*, 419, L27
- Blumenthal G. R., Gould R. J., 1970, *Rev. Mod. Phys.*, 42, 237
- Bykov A. M., 1999, in Ramaty R., Vangioni-Flam E., Cassé M., Olive K., eds, *ASP Conf. Ser. Vol. 171, LiBeB Cosmic Rays and Related X- and Gamma-Rays*, Astron. Soc. Pac., San Francisco, p. 146
- Bykov A. M., Toptygin I. N., 2001, *Ast. Lett.*, 27, 735
- Chen W., White R. L., 1994, *ApJ*, *Ap&SS*, 221, 259
- Chesneau O., et al., 2005, *A&A*, 435, 1061
- Chevalier R. A., Clegg A. W., 1985, *Nature*, 317, 44
- Cohen D. H., Leutenegger M. A., Grizzard K. T., Reed C. L., Kramer R. B., Owocki S. P., 2006, *MNRAS*, accepted
- Coker R. F., Melia F., 1997, *ApJ*, 488, L149
- Coker R. F., Pittard J. M., 2005, in Sjouwerman L. O., Dyer K. K., eds, *X-Ray and Ra-*

- dio Connections, published electronically by NRAO, <http://www.aoc.nrao.edu/events/xraydio>
- Crocker R. M., Fatuzzo M., Jokipii J. R., Melia F., Volkas R. R., 2005, *ApJ*, 622, 892
- Crowther P. A., Hillier D. J., Evans C. J., Fullerton A. W., De Marco O., Willis A. J., 2002, *ApJ*, 579, 774
- Cuadra J., Nayakshin S., Springel V., Di Matteo T., 2006, *MNRAS*, 366, 358
- De Becker M., et al., 2004a, *A&A*, 420, 1061
- De Becker M., Rauw G., Pittard J. M., Antokhin I. I., Stevens I. R., Gosset E., Owocki S. P., 2004b, *A&A*, 416, 221
- De Becker M., Rauw G., Blomme R., Pittard J. M., Stevens I. R., Runacres M. C., 2005, *A&A*, 437, 1029
- De Becker M., Rauw G., Sana H., Pollock A. M. T., Pittard J. M., Blomme R., Stevens I. R., Van Loo S., 2006, *A&A*, submitted
- De Becker M., 2005, PhD thesis, Université de Liège
- Decourchelle A., Ellison D. C., Ballet J., 2000, *ApJ*, 543, L57
- Dessart L., Crowther P. A., Hillier D. J., Willis A. J., Morris P. W., van der Hucht K. A., 2000, *MNRAS*, 315, 407
- Dessart L., Owocki S. P., 2003, *A&A*, 406, L1
- Domingo-Santamaría E., Torres D. F., 2006, *A&A*, 448, 613
- Dougherty S. M., Beasley A. J., Claussen M. J., Zauderer B. A., Bolingbroke N. J., 2005, *ApJ*, 623, 447
- Dougherty S. M., Pittard J. M., Kasian L., Coker R. F., Williams P. M., Lloyd H. M., 2003, *A&A*, 409, 217
- Dougherty S. M., Williams P. M., 2000, *MNRAS*, 319, 1005
- Dougherty S. M., Williams P. M., Pollacco D. L., 2000, *MNRAS*, 316, 143
- Draine B. T., McKee C. F., 1993, *ARA&A*, 31, 373
- Dwarkadas V. V., Owocki S. P., 2002, *ApJ*, 581, 1337
- Eenens P. R. J., Williams P. M., 1992, *MNRAS*, 255, 227
- Eichler D., Usov V., 1993, *ApJ*, 402, 271
- Ellison D. C., Baring M. G., Jones F. C., 1995, *ApJ*, 453, 873
- Ellison D. C., Baring M. G., Jones F. C., 1996, *ApJ*, 473, 1029
- Ellison D. C., Cassam-Chenaï G., 2005, *ApJ*, 632, 920
- Ellison D. C., Decourchelle A., Ballet J., 2004, *A&A*, 413, 189
- Ellison D. C., Decourchelle A., Ballet J., 2005, *A&A*, 429, 569
- Ellison D. C., Drury L. O'C., Meyer J.-P., 1997, *ApJ*, 487, 197
- Ellison D. C., Jones F. C., Baring M. G., 1999, *ApJ*, 512, 403
- Figier D. F., Kim S. S., Morris M., Serabyn E., Rich R. M., McLean I. S., 1999, *ApJ*, 525, 750
- Figier D. F., McLean I. S., Morris M., 1999, *ApJ*, 514, 202
- Fullerton A. W., Massa D. L., Prinja R. K., 2005, preprint (astro-ph/0510252)
- Gayley K. G., Owocki S. P., Cranmer S. R., 1997, *ApJ*, 475, 786
- Ghez A. M., et al., 2005, *ApJ*, 620, 744
- Hartman R. C., et al., 1999, *ApJS*, 123, 79
- Henley D. B., 2005, PhD thesis, Univ. Birmingham
- Henley D. B., Stevens I. R., Pittard J. M., 2003, *MNRAS*, 346, 773
- Herrero A., Puls J., Najarro F., 2002, *A&A*, 396, 949
- Hillas, A. M., 2005, *Journal of Physics G Nuclear Physics*, 31, 95
- Hillier D. J., Miller D. L., 1999, *ApJ*, 519, 354
- Hillier D. J., Lanz T., Heap S. R., Hubeny I., Smith L. J., Evans C. J., Lennon D. J., Bouret J. C., 2003, *ApJ*, 588, 1039
- Horns D., 2005, *Phys. Letters*, B607, 225
- Jardine M., Allen H. R., Pollock A. M. T., 1996, *A&A*, 314, 594
- Jokipii J. R., 1987, *ApJ*, 313, 842
- Kirk J. G., Heavens A. F., 1989, *MNRAS*, 239, 995
- Koch H. W., Motz J. W., 1959, *Rev. Mod. Phys.*, 31, 920
- Longair M. S., 1994, *High Energy Astrophysics*, Vol. 2 (2nd ed.). Cambridge Univ. Press, Cambridge, UK
- Marchenko S. V., Moffat A. F. J., Vacca W. D., Côté S., Doyon R., 2002, *ApJ*, 565, L59
- Marchenko S. V. et al., 2003, *ApJ*, 596, 1295
- Massa D., Fullerton A. W., Sonneborn G., Hutchings J. B., 2003, *ApJ*, 586, 996
- Mayer-Hasselwander H. A., et al., 1998, *A&A*, 335, 161
- Melrose D. B., Crouch A., 1997, *PASA*, 14, 251
- Mewe R., Kaastra J. S., Liedahl D. A., 1995, *Legacy*, 6, 16
- Meyer J.-P., Drury L. O'C., Ellison D. C., 1997, *ApJ*, 487, 182
- Moffat A. F. J., et al., 2002, *ApJ*, 573, 191
- Mullan D. J., Waldron W. L., 2006, *ApJ*, 2006, 637, 506
- Muno M. P., et al., 2004, *ApJ*, 613, 326
- Naito T., Takahara F., 1995, *MNRAS*, 275, 1077
- Orth C. D., Buffington A., 1976, *ApJ*, 206, 312
- Oskinova L., 2005, *MNRAS*, 361, 679
- Owocki S. P., Castor J. I., Rybicki G. B., 1988, *ApJ*, 335, 914
- Owocki S. P., Cohen D. H., 2006, *ApJ* accepted
- Ozernoy L. M., Genzel R., Usov V. V., 1997, *MNRAS*, 288, 237
- Quataert E., Loeb A., 2005, *ApJ*, 635, L45
- Perley R. A., Taylor G. B., 2003, in *The VLA Calibrator Manual* (<http://www.aoc.nrao.edu/~gtaylor/calib.html>)
- Petschek H. E., 1964, in Ness W. N., ed., *The Physics of Solar Flares*. NASA SP-50, 425
- Pittard J. M., Corcoran M. F., 2002, *A&A*, 383, 636
- Pittard J. M., Dougherty S. M., Coker R. F., O'Connor E., Bolingbroke N. J., 2006, *A&A*, 446, 1001
- Pittard J. M., Stevens I. R., 2002, *A&A*, 388, L20
- Pittard J. M., Stevens I. R., Williams P. M., Pollock A. M. T., Skinner S. L., Corcoran M. F., Moffat A. F. J., 2002, *A&A*, 388, 335
- Pollock A. M. T., Corcoran M. F., Stevens I. R., 2002, in Moffat A. F. J., St-Louis N., eds, *ASP. Conf. Ser. Vol. 260, Interacting Winds from Massive Stars*. Astron. Soc. Pac., San Francisco, p. 537
- Pollock A. M. T., Corcoran M. F., Stevens I. R., Williams P. M., 2005, *ApJ*, 629, 482
- Pope M. H., Melrose D. B., 1994, *PASA*, 11, 175
- Priest E., Forbes T., 2000, *Magnetic Reconnection: MHD Theory and Applications*. Cambridge Univ. Press, Cambridge, UK
- Raga A. C., Velázquez P. F., Cantó J., Masciadri E., Rodríguez L. F., 2001, *ApJ*, 559, L33
- Rakowski C. E., 2005, *Adv. Space Res.*, 35, 1017
- Reimer A., Pohl M., Reimer O., 2005, preprint (astro-ph/0510701)

- Repolust T., Puls J., Herrero A., 2004, *A&A*, 415, 349
- Rockefeller G., Fryer C. L., Baganoff F. K., Melia F., 2005, *ApJ*, 635, L141
- Romero G. E., Benaglia P., Torres D. F., 1999, *A&A*, 348, 868
- Schlickeiser R., 1984, *A&A*, 136, 227
- Silich S., Tenorio-Tagle G., Rodríguez-González A., 2004, *ApJ*, 610, 226
- Smith N., 2002, *MNRAS*, 337, 1252
- Stevens I. R., Hartwell J. M., 2003, *MNRAS*, 339, 280
- Stevens I. R., Pollock A. M. T., 1994, *MNRAS*, 269, 226
- Torres D. F., Domingo-Santamaría E., Romero G. E., 2004, *ApJ*, 601, L75
- Tuthill P. G., Monnier J. D., Danchi W. C., 1999, *Nature*, 398, 487
- Van Hoof P. A. M., Martin P. G., Ferland G. J., 2000, in Franco J., Terlevich L., Lopez-Cruz O., Aretxaga I., eds, *ASP Conf. Ser. Vol. 215, Cosmic Evolution and Galaxy Formation: Structure, Interactions, and Feedback*. Astron. Soc. Pac., San Francisco, p. 220
- Van Loo S., Runacres M. C., Blomme R., 2006, *A&A*, in press
- Varricatt W. P., Williams P. M., Ashok N. M., 2004, *MNRAS*, 351, 1307
- Viotti R. F., Antonelli L. A., Rossi C., Rebecchi S., 2004, *A&A*, 420, 527
- White R. L., Becker R. H., 1995, *ApJ*, 451, 352
- Williams P. M., 1996, *RevMexAA (Ser. de Conf.)*, 5, 47
- Williams P. M., van der Hucht K. A., Pollock A. M. T., Florkowski D. R., van der Woerd H., Wamsteker W. M., 1990, *MNRAS*, 243, 662
- Williams P. M., Dougherty S. M., Davis R. J., van der Hucht K. A., Bode M. F., Setia Gunawan D. Y. A., 1997, *MNRAS*, 289, 10
- Woosley S. E., Heger A., 2006, *ApJ*, 637, 914
- Yusef-Zadeh F., 2003, *ApJ*, 598, 325
- Yusef-Zadeh F., Nord M., Wardle M., Law C., Lang C., Lazio T. J. W., 2003, *ApJ*, 590, L103
- Zhekov S. A., Skinner S. L., 2000, *ApJ*, 538, 808